相关支撑材料目录

1. 正文内容相关图片与表格
2. 国科大校部 2020 年度大学生创新实践项目计划批准立项项目名单
3. 国科大校部 2021 年度大学生创新实践项目计划批准立项项目名单
4. 国科大校部 2022 年度大学生创新实践训练计划批准立项项目名单
5. 国科大校部 2023 年度大学生创新实践训练计划项目批准立项项目名单
6. 2024 年中国科学院大学本科生创新训练计划立项项目
7. 2025 年中国科学院大学本科生创新训练计划立项项目
8. 2023 年度北京市自然科学基金本科生“启研”计划拟资助项目清单
9. 2024 年度北京市自然科学基金本科生“启研”计划拟资助项目清单
10. 2025 年度北京市自然科学基金本科生“启研”计划拟资助项目清单
11. 2024 年第十三届全国大学生化学实验竞赛三等奖-胡秋頔
12. 2024 年第十三届全国大学生化学实验竞赛三等奖-李彧涵
13. 2025 年第五届全国大学生化学实验创新设计大赛华北赛区二等奖-高文儒、杨阳、周雨沛
14. 2025 年第五届全国大学生化学实验创新设计大赛华北赛区三等奖-綦俊皓、孙元初、李紫眸
15. 向方杰访学实践工作证明
16. 向方杰访学实践报告
17. 2023 年“拔尖计划 2.0 化学研讨会”参会照片
18. 2024 年北京市优秀毕业论文指导老师证书-陈祥雨
19. 2024 年北京市优秀毕业论文证书-廖鹏崴
20. 廖鹏崴以共同第一作者发表的学术论文

正文包含图片与表格

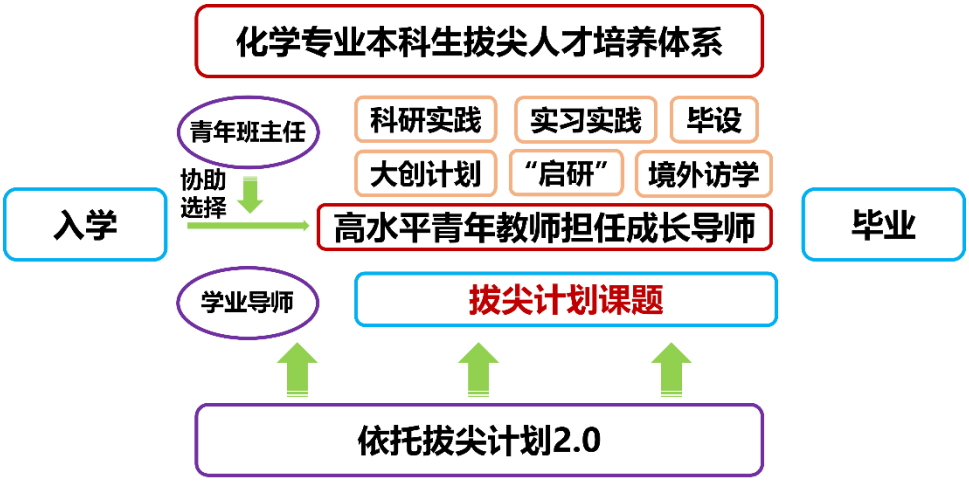

图 1. 化学专业本科生拔尖人才培养体系示意图

表 1. 优秀青年教师队伍建设

序号	姓名	所属领域	职位	人才称号	入职年份
1	张凤娇	物化	教授	青年千人	2019
2	王登超	分析	教授	中科院百人计划	2019
3	楚甲祥	无机	副教授	青年千人	2020
4	陈祥雨	有机	教授	青年千人	2020
5	倪振杰	物化	副教授	中科院百人计划	2020
6	彭谦	物化	特聘教授	杰青	2020
7	王洋	高分子	副教授	中科院百人计划	2021
8	赵达	有机	副教授	青年千人	2021
9	伦正言	材料	副教授	海外优青	2022
10	杨吉民	有机	副教授	海外优青	2023
11	孙宪虎	材料	副教授	海外优青	2023
12	姜玮	高分子	教授	优青	2025
13	高月泽	高分子	副教授	海外优青	2025

表 2. 成长导师指导本科生统计

年份	环节	参与学生总人数	学院教师指导学生人数	详情
2020	2018 级科研实践训练	28	3	刘一学（崔巍），张慧杰（齐婷），吕成磊（齐婷）
	2017 级实习实践	27	0	
	2016 级毕业论文	34	0	
2021	2019 级科研实践训练	25	11	李超龙（吴丽），张子瑄（齐婷），王子曰（楚甲祥），王诗博（李保林），滕浩男（齐婷），姚兴宇（李保林），伍偲（张凤娇），李宁政（崔巍），江子昂（楚甲祥），葛宇涛（楚甲祥），曾民权（张凤娇）
	2018 级实习实践	30	1	刘一学（汪志祥）
	2017 级毕业论文	30	0	
2022	2020 级科研实践训练	19	7	廖鹏崴（陈祥雨），丁德山（赵达），贺诗梦（赵达），吕轩博（陈祥雨），唐瑜璟（徐庆岭），朱奕桥（陈祥雨），庄乐遥（陈祥雨）
	2019 级实习实践	23	4	程敬群（吴丽），金麒生（汪志祥），李超龙（吴丽），江子昂（楚甲祥）
	2018 级毕业论文	29	1	刘一学（汪志祥）
2023	2021 级科研实践训练	18	8	尤梓羽（伦正言），胡之源（伦正言），师帅安（赵达），王伟光（倪振杰），

				胡秋頓(倪振杰),刘鋆(王登超），王凯扬（王洋），魏月华（陈凯凯）
	2020 级实习实践	18	1	廖鹏崴（陈祥雨）
	2019 级毕业论文	22	1	江子昂（楚甲祥）
2024	2022 级科研实践训练	26	7	余仁杰（伦正言），綦俊皓（倪振杰），郭志清（伦正言），陈厚谕（王洋），孙元初（王洋），陈启睿（伦正言），李昶甫（彭谦）
	2021 级实习实践	16	4	尤梓羽（伦正言），胡之源（伦正言），陈卓（张银龙），乐天（欧阳涵）
	2020 级毕业论文	21	3	向方杰（伦正言），廖鹏崴（陈祥雨），罗程炜（陈凯凯）
2025	2021 级毕业论文	16	5	尤梓羽（伦正言），胡之源（伦正言），毛臻康（王登超），陈卓（张银龙），乐天（欧阳涵）

表 3. 2020-2025 年大创项目列表

序号	年度	学生姓名	项目名称	指导教师
1	2020	邹天维	多并噻吩的合成及其性质研究	李保林
2	2020	雷德民	电化学（电池及低能耗发电装置）	张占军
3	2020	张慧杰	C-N 偶联反应优化	齐婷
4	2020	徐千贺	石墨烯及二维 COF 材料光电器件研究	杨志勇
5	2020	王子曰	金属有机配合物活化氮气研究	楚甲祥
6	2021	金麒生	基于分子模拟和多元统计方法的功能材料设计	崔巍
7	2021	雷德民	绿色发电机市场化初步研究（电化学方向）	张占军
8	2021	刘一学	膦键催化剂的设计合成与应用	陈祥雨
9	2021	程敬群	功能核酸对靶蛋白的降解	吴丽
10	2021	伍偲	有机场效应晶体管的大面积制备与化学传感应用研究	张凤娇
11	2021	张子瑄	有机光电材料的合成与表征	齐婷
12	2021	王诗博	并三噻吩化合物的合成及性质研究	李保林
13	2022	修仕帅	高性能有机光伏材料的合成	倪振杰
14	2022	黄可夫	有机光电理论、模拟与计算	彭谦
15	2022	丁德山	新型氟-18 探针的合成与标记	赵达
16	2022	雷德民	废弃电池回收处理及利用（一）	张占军
17	2022	廖鹏崴	电子给-受体复合物促使的氟甲基化反应	陈祥雨
18	2022	唐瑜璟	新型过氧化氢荧光探针与生物成像	徐庆岭
19	2022	程敬群	控制核酸分子中偶氮苯开关的分子因素	吴丽
20	2022	何炎	抗肿瘤血管新生纳米药物的制备	张银龙
21	2023	廖鹏崴	可见光诱导硫键促使的碳-磷键构建	陈祥雨
22	2023	尤梓羽	富锂锰基高熵正极的设计与优化	伦正言
23	2023	刘鋆	双金属纳米材料的合成与催化水分解性能研究	赵红
24	2023	王凯扬	锂电池与燃料电池光电展示模型开发与制造	王雪飞
25	2023	王伟光	有机发光晶体管关键材料制备及表征的探索	倪振杰
26	2023	孙明康	废弃电池回收处理及利用	张占军

27	2023	王雅芹	手性有机发光材料的设计与合成	齐婷
28	2023	蒲泽暄	Arduino 应用研究	崔巍
29	2023	魏月华	纳米孔芯片的创制与测试	陈凯凯
30	2023	陈卓	抗血小板药物纳米逆转剂制备及其应用研究	张银龙
31	2023	乐天	生物可吸收电子器械	欧阳涵
32	2024	胡之源	阳离子半局域无序尖晶石正极材料的设计与合成	伦正言
33	2025	潘政熹	面向高比能锂电池的锰基无序阳离子正极全电池体系研究	伦正言
34	2025	陈启睿	聚合物固态电解质的设计、表征与合成	伦正言
35	2025	张昀沛	基于氧杂蒽骨架的新型低价稀土配合物的合成及反应性研究	楚甲祥

表 4. 北京市自然科学基金“启研”计划项目列表

序号	年度	学生姓名	项目名称	指导老师
1	2023	廖鹏崴	可见光诱导硫键促使的碳磷键构建	陈祥雨
2	2023	孙海洋	钠离子电池正极材料表面控制与空气稳定性研究	曹安民
3	2023	李彧涵	温和条件下由氮气与卤代物合成有机胺	王从洋
4	2023	尤梓羽	富锂高熵无序岩盐正极材料失效机理研究及性能优化	伦正言
5	2023	陈卓	血小板仿生纳米颗粒逆转抗血小板药物药效研究	张银龙
6	2024	郭炆京	微纳液滴操控图案化用于高通量构建类器官阵列芯片研究	宋延林
7	2024	陆蓥川	时空特异性基因编辑的化学生物学研究	汪铭
8	2024	郭志清	基于局域等离子共振效应的高量子产率光催化剂设计	唐智勇
9	2025	潘政熹	基于锰基阳离子无序型正极的高比能锂离子全电池构筑	伦正言
10	2025	陈厚谕	过渡金属促进的电化学氮气活化与有机转化	王从洋

国科大校部2020年度大学生创新实践项目计划批准立项项目名单

项目编号	项目申请号	学生姓名	学生所在院校	项目名称	指导教师姓名	指导教师所在院系	项目资助金额（万元）	项目执行期限
26	20204000395	邹天维	中国科学院大学	多并噻吩的合成及其性质研究	李保林	化学学院	1.77	2020/6-2021/12
27	20204000428	雷德民	中国科学院大学	电化学（电池及低能耗发电装置）	张占军	化学学院	1.77	2020/6-2021/12
31	20204001153	张慧杰	中国科学院大学	C-N偶联反应优化	齐婷	化学学院	1.77	2020/6-2021/12
32	20204001577	徐千贺	中国科学院大学	石墨烯及二维COF材料光电器件研究	杨志勇	化学学院	1.77	2020/6-2021/12
33	20204001590	王子曰	中国科学院大学	金属有机配合物活化氮气研究	楚甲祥	化学学院	1.77	2020/6-2021/12

国科大校部2021年度大学生创新实践项目计划批准立项项目名单

项目编号	项目申请号	学生姓名	学生所在院校	项目名称	指导教师姓名	指导教师所在院系	项目资助金额（万元）	项目执行期限
20	20214000772	金麒生	中国科学院大学	基于分子模拟和多元统计方法的功能材料设计	崔巍	化学科学学院	1.8	2021-7-1日至2022-6-30
23	20214000971	雷德民	中国科学院大学	绿色发电机市场化初步研究（电化学方向）	张占军	化学科学学院	1.8	2021-7-1日至2022-6-30
26	20214000883	刘一学	中国科学院大学	膦键催化剂的设计合成与应用	陈祥雨	化学科学学院	1.8	2021-7-1日至2022-6-30
27	20214001217	程敬群	中国科学院大学	功能核酸对靶蛋白的降解	吴丽	化学科学学院	1.8	2021-7-1日至2022-6-30
28	20214001003	伍偲	中国科学院大学	有机场效应晶体管的大面积制备与化学传感应用研究	张凤娇	化学科学学院	1.8	2021-7-1日至2022-6-30
29	20214001120	张子瑄	中国科学院大学	有机光电材料的合成与表征	齐婷	化学科学学院	1.8	2021-7-1日至2022-6-30
30	20214001151	王诗博	中国科学院大学	并三噻吩化合物的合成及性质研究	李保林	化学科学学院	1.8	2021-7-1日至2022-6-30

国科大校部2022年度大学生创新实践训练计划批准立项项目名单

项目	项目申请号	学生姓名	学生所在院校	项目名称	指导教师姓名	指导教师所在院系	项目资助金额（万元）	项目执行期限
24	20224000239	修仕帅	中国科学院大学	高性能有机光伏材料的合成	倪振杰	中国科学院大学化学科学学院	1.9	2022年7月1日-2023年8月31日
28	20224000917	黄可夫	中国科学院大学	有机光电理论、模拟与计算	彭谦	中国科学院大学化学科学学院	1.9	2022年7月1日-2023年8月31日
29	20224000461	丁德山	中国科学院大学	新型氟-18探针的合成与标记	赵达	中国科学院大学化学科学学院	1.9	2022年7月1日-2023年8月31日
31	20224001476	雷德民	中国科学院大学	废弃电池回收处理及利用（一）	张占军	中国科学院大学化学科学学院	1.9	2022年7月1日-2023年8月31日
33	20224000847	廖鹏崴	中国科学院大学	电子给-受体复合物促使的氟甲基化反应	陈祥雨	中国科学院大学化学科学学院	1.9	2022年7月1日-2023年8月31日
35	20224001179	唐瑜璟	中国科学院大学	新型过氧化氢荧光探针与生物成像	徐庆岭	中国科学院大学化学科学学院	1.9	2022年7月1日-2023年8月31日
36	20224001470	程敬群	中国科学院大学	控制核酸分子中偶氮苯开关的分子因素	吴丽	中国科学院大学化学科学学院	1.9	2022年7月1日-2023年8月31日
60	20224000641	何炎	中国科学院大学	抗肿瘤血管新生纳米药物的制备	张银龙	中国科学院大学纳米科学与技术学院	1.8	2022年7月1日-2023年8月31日

国科大校部2023年度大学生创新实践训练计划项目申请名单

序号	申请号	姓名	学校名称	项目名称	指导教师	培养单位	资助经费（万元）	项目执行期限
70	20234000118	魏月华	中国科学院大学	纳米孔芯片的创制与测试	陈凯凯	中国科学院大学纳米科学与工程学院	1.76	2023年9月-2024年9月
71	20234000275	陈卓	中国科学院大学	抗血小板药物纳米逆转剂制备及其应用研究	张银龙	中国科学院大学纳米科学与工程学院	1.76	2023年9月-2024年9月
72	20234000807	乐天	中国科学院大学	生物可吸收电子器械	欧阳涵	中国科学院大学纳米科学与工程学院	1.76	2023年9月-2024年9月
102	20234000099	廖鹏崴	中国科学院大学	可见光诱导硫键促使的碳-磷键构建	陈祥雨	中国科学院大学化学科学学院	1.86	2023年9月-2024年9月
103	20234000472	尤梓羽	中国科学院大学	富锂锰基高熵正极的设计与优化	伦正言	中国科学院大学化学科学学院	1.86	2023年9月-2024年9月
104	20234000353	刘鎏	中国科学院大学	双金属纳米材料的合成与催化水分解性能研究	赵红	中国科学院大学化学科学学院	1.86	2023年9月-2024年9月
106	20234000218	王凯扬	中国科学院大学	锂电池与燃料电池光电展示模型开发与制造	王雪飞	中国科学院大学化学科学学院	1.86	2023年9月-2024年9月
107	20234000413	王伟光	中国科学院大学	有机发光晶体管关键材料制备及表征的探索	倪振杰	中国科学院大学化学科学学院	1.86	2023年9月-2024年9月
113	20234000926	孙明康	中国科学院大学	废弃电池回收处理及利用	张占军	中国科学院大学化学科学学院	1.86	2023年9月-2024年9月
114	20234000968	王雅芹	中国科学院大学	手性有机发光材料的设计与合成	齐婷	中国科学院大学化学科学学院	1.86	2023年9月-2024年9月
115	20234000892	蒲泽暄	中国科学院大学	Arduino应用研究	崔巍	中国科学院大学化学科学学院	1.86	2023年9月-2024年9月

2024 年中国科学院大学本科生创新训练计划立项项目

序号	学院	项目级别	项目编号	项目名称	项目负责人姓名	指导教师姓名	支持经费(元)
10	化学科学学院	市级	S202414430010	阳离子半局域无序尖晶石正极材料的设计与合成	胡之源	伦正言	40000
17	化学科学学院	校级	X202414430017	高分子膜负载的液膜忆阻器制备与应用	施心琪	于萍	20000
18	化学科学学院	校级	X202414430018	光催化甲烷转化	郭志清	唐智勇	20000

2025年中国科学院大学本科生创新训练计划立项项目

序号	院系	项目级别	项目编号	项目名称	项目负责人姓名	指导教师姓名	支持经费（元）
4	化学科学学院	国家级	202514430004	微纳液滴操控图案化用于高通量构建类器官阵列芯片研究	郭炆京	宋延林	40000
5	化学科学学院	市级	S202514430005	高容量富锂锰基正极材料的合成及动力学性能研究	魏于斌	石吉磊	40000
9	化学科学学院	校级	X202514430009	面向高比能锂电池的锰基无序阳离子正极全电池体系研究	潘政熹	伦正言	20000
10	化学科学学院	校级	X202514430010	废弃PET高值定向转化为可降解高性能聚酯	张旭东	董侠	20000
11	化学科学学院	校级	X202514430011	聚合物固态电解质的设计、表征与合成	陈启睿	伦正言	20000
12	化学科学学院	校级	X202514430012	基于氧杂蒽骨架的新型低价稀土配合物的合成及反应性研究	张昀沛	楚甲祥	20000

附件 1

2023 年度北京市自然科学基金本科生“启研”计划拟资助项目清单

单位：万元

序号	拟资助编号	项目名称	依托单位	申请人	拟资助经费
1	QY23154	哈密顿圈问题的量子算法设计	中国科学院大学	李蕊	6.7
2	QY23155	多级轴流压气机导/静叶可调规律的数据挖掘优化	中国科学院大学	孟繁星	5.4
3	QY23156	神经网络的鲁棒记忆能力及鲁棒泛化性探究	中国科学院大学	邱瑞晨	3.3
4	QY23157	气动-推进多学科耦合伴随梯度优化设计方法研究	中国科学院大学	林涛	3.3
5	QY23158	高超声速气动布局隐身耦合优化研究	中国科学院大学	唐烨晨	5.4
6	QY23159	节点覆盖统计物理问题的图神经网络方法	中国科学院大学	李田	3.3
7	QY23160	拓扑超导体 PtPb4 超导能隙与反常输运性质的角分辨光电子能谱研究	中国科学院大学	张振昊	6.7
8	QY23161	石墨烯摩尔超晶格中等离激元的探测与调控	中国科学院大学	张笑晗	3.3
9	QY23162	双锥对撞点火方案中的热斑形成与自组织聚变燃烧研究	中国科学院大学	王美乔	5.9
10	QY23163	基于机器学习的新型低维无定形材料的力学性质研究	中国科学院大学	李诗语	3.3
11	QY23164	大型强子对撞机底夸克实验上双电荷四夸克态性质的研究	中国科学院大学	毛胜寒	3.3
12	QY23165	利用非线性光学技术研究自支撑氧化物薄膜的原位应变调控	中国科学院大学	王艺儒	5.4
13	QY23166	LHCb 上的双粲重子实验研究	中国科学院大学	韩书钰	6.7
14	QY23167	离子量子计算平台中长离子链多普勒冷却激光优化方案	中国科学院大学	华文翰	6.7
15	QY23168	电荷宇称破坏相角 γ 测量新方法的探索研究	中国科学院大学	耿靖博	3.3
16	QY23169	可见光诱导硫键促使的碳磷键构建	中国科学院大学	廖鹏崴	3.3
17	QY23170	钠离子电池正极材料表面控制与空气稳定性研究	中国科学院大学	孙海洋	3.3
18	QY23171	温和条件下由氮气与卤代物合成有机胺	中国科学院大学	李彧涵	6.7

序号	拟资助编号	项目名称	依托单位	申请人	拟资助经费
19	QY23172	片上可集成光量子器件(集成分束器和滤波器等设计与制备)	中国科学院大学	谭世卓	6.7
20	QY23173	原位合金化无锌负极材料的构筑与成核机理研究	中国科学院大学	陈心怡	6.7
21	QY23174	晶圆级 GeOI 异质集成工艺及制作研究	中国科学院大学	段晓丰	3.3
22	QY23175	高电压钴酸锂正极材料结构调控与构效关系研究	中国科学院大学	朱天宇	6.7
23	QY23176	富锂高熵无序岩盐正极材料失效机理研究及性能优化	中国科学院大学	尤梓羽	6.7
24	QY23177	高性能波导耦合性硅基 Ge 高饱和光电探测器	中国科学院大学	王雅芹	6.7
25	QY23178	极低抖动低功耗锁相环时钟生成集成电路设计技术的研究	中国科学院大学	肖亚东	6.1
26	QY23179	基于概率扩散模型的对抗扰动净化技术研究	中国科学院大学	黄玥绮	3.3
27	QY23180	面向国产 DCU 加速器和 AMD GPU 的卷积算子编译优化方法研究	中国科学院大学	向佳为	3.3
28	QY23181	面向近存计算的领域专用计算关键技术研究	中国科学院大学	杨帆	4.0
29	QY23182	基于扩散模型的高帧间一致性的长视频生成	中国科学院大学	景石柔	6.7
30	QY23183	面向复杂拓扑结构的三维模型生成方法研究	中国科学院大学	魏歆哲	6.7
31	QY23184	基于龙架构的高性能浮点部件设计与优化	中国科学院大学	刘子扬	3.3
32	QY23185	面向移动设备的高真实感的实时三维重建技术	中国科学院大学	廖安旭	6.7
33	QY23186	小尺度目标识别与跨时空关联	中国科学院大学	曾建树	4.0
34	QY23187	面向小样本、大场景激光点云的几何拓扑增强深度神经网络研究	中国科学院大学	林诚皓	6.7
35	QY23188	基于毫米波雷达的 SLAM 技术	中国科学院大学	戴小龙	5.1
36	QY23189	超宽带光通信驱动电路设计	中国科学院大学	徐亦周	3.3
37	QY23190	复制叉处核小体组装与 DNA 复制偶联的结构机理	中国科学院大学	孙骥	6.7
38	QY23191	血小板仿生纳米颗粒逆转抗血小板药物药效研究	中国科学院大学	陈卓	5.4
39	QY23192	北京城市公共交通网络连通性评价及优化方案	中国科学院大学	丁钰航	3.3
40	QY23193	基于低碳目标的北京市能源消费结构优化路径解析	中国科学院大学	戴亦杨	3.3

附件 1

2024 年度北京市自然科学基金本科生“启研”计划拟资助项目清单

单位：万元

序号	拟资助编号	项目名称	依托单位	申请人	拟资助经费
1	QY24353	图像检索问题在量子计算框架下的优化模型表示与算法设计	中国科学院大学	闫项尧	5.4
2	QY24354	情境学习的收敛速率和有限步累积遗憾上界的分析与优化	中国科学院大学	李高远	3.5
3	QY24355	史瓦西型度量上波方程球对称解的适定性研究	中国科学院大学	黄胤翰	3.5
4	QY24356	力学可控的三维管状支气管芯片开发及在力学调控病毒入侵中的应用	中国科学院大学	朱崇源	4.8
5	QY24357	变构型高超声速飞机气动特性分析和优化设计	中国科学院大学	廖家豪	5.4
6	QY24358	Td 相 MoTe2 中超导铁电共存性的实验研究	中国科学院大学	张萌珊	3.5
7	QY24359	钯基负载的超快速声表面波(SAW)氢敏机理及器件优化研究	中国科学院大学	黄林泰辉	6.2
8	QY24360	LHCb 实验上的奇特强子态研究	中国科学院大学	郭庆翔	6.9
9	QY24361	高能电子点燃高密度燃料后的 D-D 聚变反应	中国科学院大学	刘一珉	6.7
10	QY24362	基于静电驱动的零偏平衡摆研究	中国科学院大学	邓昊烨	3.5
11	QY24363	基于量子计算特性的一种机器学习算法研究及其复杂度算法的一般性推广	中国科学院大学	蒲实	3.3
12	QY24364	基于 MicroMegas 的 CEvNS 方向性探测	中国科学院大学	余运林晨	6.9
13	QY24365	连带活性布朗粒子模型运动模式探索	中国科学院大学	张智恒	5.4
14	QY24366	利用立体水切伦科夫探测器对百 GeV 伽马射线观测方法的优化研究	中国科学院大学	厉艺阳	3.5
15	QY24367	MARVEL 实验的低气压 GMPD 探测器研究	中国科学院大学	左杰	6.9
16	QY24368	光激发二维材料中的非线性声子计算	中国科学院大学	林珉童	3.5
17	QY24369	转角石墨烯的精准构筑及莫尔超晶格研究	中国科学院大学	高瑗琪	3.5

序号	拟资助编号	项目名称	依托单位	申请人	拟资助经费
18	QY24370	时空特异性基因编辑的化学生物学研究	中国科学院大学	陆鋆川	6.9
19	QY24371	利用局域表面等离子共振效应实现高量子产率的可见光催化甲烷部分氧化	中国科学院大学	郭志清	6.9
20	QY24372	自组装构建Cu-DNAzyme杂合型纳米材料及抗肿瘤研究	中国科学院大学	王良国	6.9
21	QY24373	微纳液滴操控图案化用于高通量构建类器官阵列芯片研究	中国科学院大学	郭炆京	3.5
22	QY24374	基于三维石墨烯结构的柔性电子皮肤传感器用于机器人触觉感知	中国科学院大学	严明达	3.5
23	QY24375	多极化合成孔径雷达与 Transformer 实现全天候作物精细分类	中国科学院大学	傅世平	6.2
24	QY24376	基于相位编码信号的合成孔径雷达成像性能比较及验证	中国科学院大学	燕晨昊	3.5
25	QY24377	基于高斯表征的数字人脸重建和驱动	中国科学院大学	孔德衍	3.5
26	QY24378	面向向量数据库的评测基准和优化研究	中国科学院大学	张雪雅	6.9
27	QY24379	基于龙架构的 CPU 张量协处理器设计与协同优化	中国科学院大学	岳俊宇	6.9
28	QY24380	基于香山处理器的向量密码学扩展指令集实现	中国科学院大学	吉骏雄	6.9
29	QY24381	面向科学智能模拟的RISC-V增强指令集研究	中国科学院大学	饶嘉怡	5.4
30	QY24382	基于可穿戴眼动交互的抑郁情感检测关键技术研究	中国科学院大学	徐天怿	6.9
31	QY24383	基于幻觉检测的一致性 3D 生成	中国科学院大学	童昊阳	3.5
32	QY24384	多模态信息引导的舞蹈生成方法研究	中国科学院大学	骆敏言	4.8
33	QY24385	基于触力觉阵列的人机精细交互技能分析方法研究	中国科学院大学	田昊洋	3.5
34	QY24386	机器人滚筒视触觉传感机理与触感建模方法研究	中国科学院大学	李贤琦	6.9
35	QY24387	面向多模态大模型的自适应泛化能力研究	中国科学院大学	胡勇冠	3.5
36	QY24388	面向芯粒间互连的高能效紧凑型时钟数据恢复电路的研究	中国科学院大学	王静扬	3.5
37	QY24389	小鼠胚胎体外长时程培养体系的建立和优化	中国科学院大学	吴庭逸	3.5
38	QY24390	衰老过程中花生四烯酸代谢通路表达变化的特征归纳和模拟	中国科学院大学	闵煜泽	3.5

序号	拟资助编号	项目名称	依托单位	申请人	拟资助经费
39	QY24391	人逆转座子LINE-1底物识别机制的结构与功能研究	中国科学院大学	王韵淇	6.9
40	QY24392	融合地理大数据和深度学习的城市功能区精准识别与空间优化：基于中欧的比较研究	中国科学院大学	尧祥临	4.1

附件 1

2025 年度北京市自然科学基金本科生“启研”计划拟资助项目清单

单位：万元

序号	拟资助编号	项目名称	依托单位	申请人	拟资助经费
1	QY25160	大模型赋能无人机自主指控智能“中间体”技术研究	中国科学院大学	戴银杏	5
2	QY25161	融合物理先验的扫描隧道显微学原子识别框架	中国科学院大学	李柏葳	4
3	QY25162	机器学习驱动的粲强子的陶轻子纯轻衰变的研究	中国科学院大学	廖飞扬	4
4	QY25163	横向热电输运的理论研究	中国科学院大学	武岚琛	4
5	QY25164	系外行星共进 Hill 半径新阈值模型及宜居环境轨道稳定性研究	中国科学院大学	杨谨睿	5
6	QY25165	AI 赋能的核坍缩型超新星的极早期光变和光谱研究	中国科学院大学	王芝懿	5
7	QY25166	在 LHCb 实验上寻找 Lambda_b 和 Xi^-重子衰变中的电荷-宇称对称性破坏	中国科学院大学	陈依翎	4
8	QY25167	面内各向异性二维半导体中光学腔和声子腔的耦合效应	中国科学院大学	李昊轩	4
9	QY25168	基于主动学习的二维翘曲非晶材料结构设计方法	中国科学院大学	张俊炜	4
10	QY25169	双锥对撞点火激光聚变方案的稳定性与效率研究	中国科学院大学	马旭	5
11	QY25170	使用 desilike 再约束暗能量状态方程	中国科学院大学	王誉寰	5
12	QY25171	基于锰基阳离子无序型正极的高比能锂离子全电池构筑	中国科学院大学	潘政熹	6
13	QY25172	过渡金属促进的电化学氮气活化与有机转化	中国科学院大学	陈厚谕	5
14	QY25173	高性能光电振荡器的智能控制系统的设计及实现	中国科学院大学	王忠钰	6
15	QY25174	生物基复合材料触觉传感成像系统研究	中国科学院大学	杨钰炜	6
16	QY25175	对面向极端环境的硅谐振压力传感器的研究	中国科学院大学	李润韬	4
17	QY25176	物理特性嵌入的合成孔径雷达智能成像	中国科学院大学	赵星宇	6

序号	拟资助编号	项目名称	依托单位	申请人	拟资助经费
18	QY25177	基于脉冲神经网络的合成孔径雷达目标检测	中国科学院大学	刘鸿宇	4
19	QY25178	基于增强大模型的智能漏洞挖掘和验证方法研究	中国科学院大学	郑翊杰	4
20	QY25179	基于差分测试的静默语义漏洞发现技术研究	中国科学院大学	姜俊彦	5
21	QY25180	复杂电路错误智能定位与修复方法研究	中国科学院大学	梁婧琪	6
22	QY25181	基于单目图像的高真实感数字人生成	中国科学院大学	刘爽	4
23	QY25182	高效大规模线性规划求解器的研究与实现	中国科学院大学	韦欣池	5
24	QY25183	面向超声机器人的影像基础模型微调与跨域诊断研究	中国科学院大学	曹林颖	5
25	QY25184	面向高效手术操控的变曲率拮抗驱动连续体机器人的设计方法研究	中国科学院大学	尚博珩	6
26	QY25185	基于多维触觉灵巧手的物体抓取与识别研究	中国科学院大学	高远	6
27	QY25186	基于强化学习与离线数据协同优化的大语言模型高效微调方法研究	中国科学院大学	陈霆鸿	5
28	QY25187	基于可控生成模型的图像结构与风格编辑	中国科学院大学	王琦琪	6
29	QY25188	视觉自回归生成模型高效优化方法的研究	中国科学院大学	潘天麟	4
30	QY25189	3DGS 动态场景建模技术研究	中国科学院大学	朱首赫	5
31	QY25190	面向片间光互连的调制器波长控制芯片研究	中国科学院大学	吴其训	4
32	QY25191	低比特量化的 Transformer 端侧大模型加速器架构设计	中国科学院大学	胡天飞雪	6
33	QY25192	基于深度学习的超分辨荧光成像技术的研究	中国科学院大学	李瑞林	6
34	QY25193	全软体动物层级化行为空间与神经控制机制研究	中国科学院大学	成修屹	4
35	QY25194	一种潜在的疫苗佐剂载体：AI 从头设计改造 A137R 自组装纳米笼颗粒	中国科学院大学	瞿浩	6
36	QY25195	HES4 基因在人类皮层发育中的作用及其物种特异性研究	中国科学院大学	何雨馨	6
37	QY25196	气味的“音高”——听觉对嗅知觉竞争现象的调节作用	中国科学院大学	邢若雨	5
38	QY25197	基于大语言模型的微博青少年用户抑郁焦虑识别及干预技术研究	中国科学院大学	唐淑怡	5

序号	拟资助编号	项目名称	依托单位	申请人	拟资助经费
39	QY25198	AlphaFold 辅助的新型表观遗传编辑系统开发	中国科学院大学	周聿玮	6

荣誉证书

HONORARY CREDENTIAL

中国科学院大学 胡秋頔同学

荣获第十三届全国大学生化学实验竞赛总决赛三等奖。

特发此证，以资鼓励。

教育部高等学校化学教育研究中心

教育部高等学校国家级实验教学示范中心联席会

二零二四年八月

荣誉证书

HONORARY CREDENTIAL

中国科学院大学 李彧涵同学

荣获第十三届全国大学生化学实验竞赛总决赛三等奖。

特发此证，以资鼓励。

教育部高等学校化学教育研究中心

教育部高等学校国家级实验教学示范中心联席会

二零二四年八月

荣誉证书

第五届全国大学生化学实验创新设计大赛“岛津杯”华北赛区竞赛

二等奖

获奖学校：中国科学院大学

作品名称：DNA编码多肽骨架的合成、分离与表征

获奖学生：高文儒 杨阳 周雨沛

教育部高等学校化学教育研究中心

教育部高等学校国家级实验教学示范中心联席会

2025年8月5日

证书号：2025-华北赛区-S095

荣誉证书

第五届全国大学生化学实验创新设计大赛“岛津杯”华北赛区竞赛

三等奖

获奖学校：中国科学院大学

作品名称：酶催化反应在DNA编码多肽的生物兼容性评价中的应用

获奖学生：綦俊皓 孙元初 李紫眸

教育部高等学校化学教育研究中心

教育部高等学校国家级实验教学示范中心联席会

2025年8月5日

证书号：2025-华北赛区-S178

UNIVERSITY OF CALIFORNIA, BERKELEY

BERKELEY • DAVIS • IRVINE • LOS ANGELES • MERCED • RIVERSIDE • SAN DIEGO • SAN FRANCISCO

SANTA BARBARA • SANTA CRUZ

Gerbrand Ceder
Samsung Distinguished Professor in Engineering
National Academy of Engineering
Department of Materials Science & Engineering
328 Hearst Memorial Mining Building MC#1760
Berkeley, CA 94720-1760

(510) 486-7193
Fax: (510) 643-5792
gceder@berkeley.edu

04/20/2023

To Whom It May Concern:

This letter is to certify that Fangjie Xiang has been offered a position at Gerbrand Ceder's group. Fangjie Xiang will be working full-time as an *undergraduate researcher.* His job will be to realize the DRX to partially disordered spinel phase transformation.

Fangjie Xiang employment start date is May 12, 2023 and end date is August 12, 2023. This position is meant to be practical training experience and will contribute to his academic objectives.

For additional information, please contact the student's supervisor, Gerbrand Ceder at gceder@lbl.gov.

Yours sincerely,

Gerbrand Ceder
Samsung Distinguished Professor in Engineering
Fellow NAE, MRS, TMS, APS

This letter is only to be used for the purpose for which it was written and is not to be disseminated for any other reason.

Explore the potential of doping Cr in $Li_{1.1}Mn_{0.8}Ti_{0.1}O_{1.9}F_{0.1}$

Intern: Fangjie Xiang

Mentor: Han-Ming Hau

Advisor: Gerbrand Ceder

Date: 2023.2.15--2023.8.7

Abstract: In lithium ion cathode materials, the transformation from disordered rocksalt (DRX) structure to spinel-like structure (Delta) is expected to improve Li migration rate as well as retention. While chromium (Cr) shows preference of tetrahedral sites at +6 state and octahedral sites at +3 state, we demonstrate that doping Cr ions in DRX hinders the DRX-to-Delta transformation, leading to a worse electrochemical performance. However, we find delithiation and heating promote the transformation at a partial delithiated state of DRX. Using a combination of electrochemical measurement, in-situ X-ray diffraction and X-ray absorption spectrometry, we identify that cathodes doped with Cr show no two-phase reaction during cycling and underlying mechanism of Cr hindering the transformation is revealed. The whole project evaluates the feasibility of doping Cr in DRX to form Delta.

Introduction

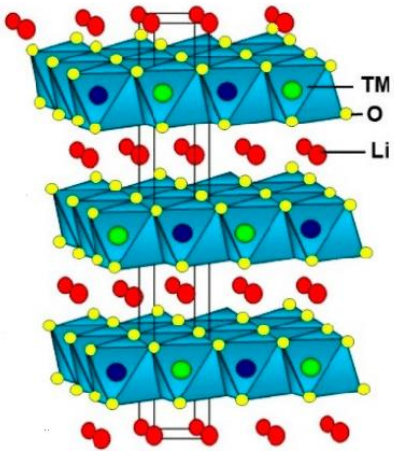

With the continuous growth in the demand of energy storage devices, Li-ion batteries become essential items in our society. Traditional Li-ion batteries adopt a layered structure (Figure 1), where Li ions occupy 3a sites and transition metals take up 3b sites. Besides, except Co, transition metals ions will migrate to different layers during cycling and lead to layered-to-spinel phase transformation. Typical slab distance for layered structures is between 2.6 and 2.7 Å, which gives a migration barriers of ~500 meV [1] .However, as the Li-ion industry is projected to grow to 1 TWh of production per year, approximately one million tons of combined cobalt and nickel will be required, which results in resource constraint[2].

Figure 1. Layered structure (NMC). TM, Li migrate in their respective layer during electrochemical cycling.

To extend the variety of transition metals that can be applied to Li-ion batteries, recent progress in the Li-excess disordered rocksalt (DRX) materials with different TM redox center has demonstrated great performance, including Fe, V, Cr etc. For example, $Li_{1.2}Nb_{0.175}Mo_{0.625}O_{1.95}F_{0.05}$ is reported to have the capacity of 275mAh/g[3]. In the DRX structure(Figure 2a), cations occupy the octahedral sites and anions occupy the FCC sites. Li hop between two octahedral sites through the intermediate tetrahedral site (*o-t-o* diffusion). Li in the intermediate tetrahedral is the activated state in Li diffusion. The activated tetrahedral Li^+ ion face-shares with four octahedral sites, and the activated energy is mostly determined by electrostatic repulsion between the activated Li^+ ion and its face-sharing species. Considering the strong electrostatic repulsion, only 0-TM (Figure 2b) channel supports the migration of Li+ ions, which involves no face-sharing TM ions[4]. By increasing Li-excess level, Li transportation can occur with cation disorder. However, high migration barrier and poor 0-TM channel percolation due to short range ordering (SRO) lead to relatively poor rate and retention.

To relieve the negative effect of SRO, Zhengyan et al. shows that increasing the configurational entropy of DRX materials by adding different TM can effectively reduce SRO[5]. Zijian et al. adopts the strategy of thermodynamically driven synthetic optimization, which successfully reduces the formation of SRO and improves the

performance of DRX by decreasing the sintering time[6].

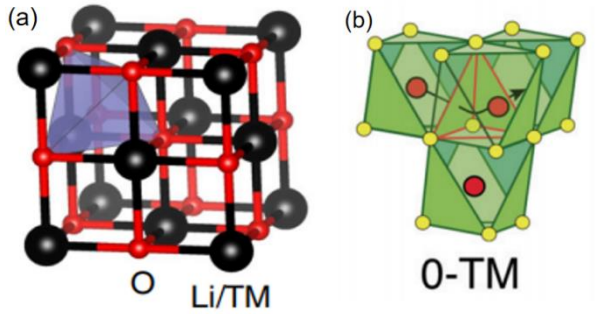

Figure 2. (a) Structure of disordered rocksalt structure (DRX), where Li and TM are distributed randomly in octahedral sites. (b) 0-TM channel, where the surrounding of tetrahedral sites are occupied by Li or vacancy.

Recent researches focusing on earth abundant high Mn-content DRX show that a disordered-to-spinel-like structure transformation in the DRX bulk surprisingly results in a capacity increase in $Li_{1.2}Ti_{0.2}Mn_{0.6}O_{0.8}F_{0.2}$ upon cycling, and the transformation may be a common phenomenon existing in high-Mn DRX cathodes[7]. The work inspires researchers to investigate the relation between DRX and spinel. Compared with DRX, spinel has intrinsic well established 0-TM channel, which leads to a better rate performance. In ordered spinel (Figure 3), the tetrahedral 8a and octahedral 16d are fully occupied by Li and TM respectively, leaving 8b and 16c sites vacant[8]. However, the two-phase reaction around 3 V plateau and the the collective 8a-to-16c Li transition in $LiMn_2O_4$ during electrochemical cycling resulting in high lattice strain between the cubic phase and a tetragonal phase, which makes the capacity of the spinel only half of its theory capacity[9].

The partially (dis)ordered spinel-like Delta phase, where TM cation occupy both the 16d and 16c sites, has been demonstrated to form from cycling high Mn-content DRX, but owns better 0-TM percolation network, retention, higher capacity due to its partially (dis)ordered spinel structure. More importantly, two-phase reaction will be converted into a solid-solution reaction[10].

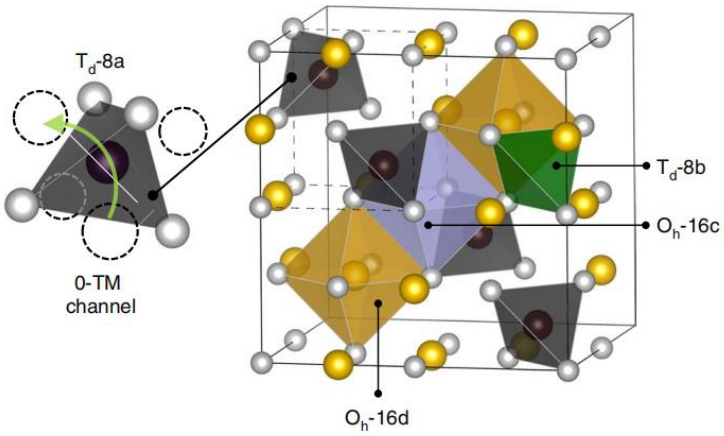

Figure 3. Crystal structure of the ordered spinel LiM_2O_4 (M = non-Li metal ions). The tetrahedral 8a and octahedral 16d are fully occupied by Li and TM, respectively.

In the study, we synthesize $Li_{1.1}Mn_{0.8}Ti_{0.1}O_{1.9}F_{0.1}$ (L11M8C0) as the pristine, which has high Mn content to realize this transformation and understand the underlying mechanism better. In this material, excess Li is necessary to form 0-TM percolation network; F is used to increase the TM-redox reservoir and suppress oxygen redox to improve retention. As an abundant d^0 element, Ti^{4+} is added to stabilize the DRX structure and acts as a charge compensator.

Further, we adopt a strategy of doping Cr. Since Cr^{3+} prefers octahedral site while Cr^{6+} prefers tetrahedral site[11], we expect the Cr oct-to-tet migration promotes the transformation from DRX to the delta phase during electrochemical cycling. Therefore,$Li_{1.1}Mn_{0.7}Cr_{0.1}Ti_{0.1}O_{1.9}F_{0.1}$ (L11M7C1) and $Li_{1.1}Mn_{0.6}Cr_{0.2}Ti_{0.1}O_{1.9}F_{0.1}$ (L11M6C2) are synthesized to investigate the effect of doping Cr ions.

Experimental section

***Material Synthesis and Electrochemical Test*:** $Li_{1.1}Mn_{0.8}Ti_{0.1}O_{1.9}F_{0.1}$ (L11M8C0), $Li_{1.1}Mn_{0.7}Cr_{0.1}Ti_{0.1}O_{1.9}F_{0.1}$ (L11M7C1) and $Li_{1.1}Mn_{0.6}Cr_{0.2}Ti_{0.1}O_{1.9}F_{0.1}$ (L11M6C2) were synthesized using the solid-state synthesis method at 1100 °C for 20 minutes. The as-synthesized particles were mixed with carbon at 7:2 through shaker-milling, and the shaker-milled sample was mixed with PTFE. The ratio for active materials: C65: PTFE = 7: 2: 1. X-ray diffraction (XRD) patterns and the corresponding Rietveld refinements in Figure 4 confirm that all three samples are rocksalt structure. The lattice parameter

of L11M8C0 is 4.160 Å. Comparing the lattice parameters of L11M7C1 and L11M6C2, we find that of L11M7C1 (4.173 Å) is larger than that of L11M6C2 (4.167 Å), which is consistent with the smaller ionic radius of Cr^{3+} compared with Mn^{3+}.

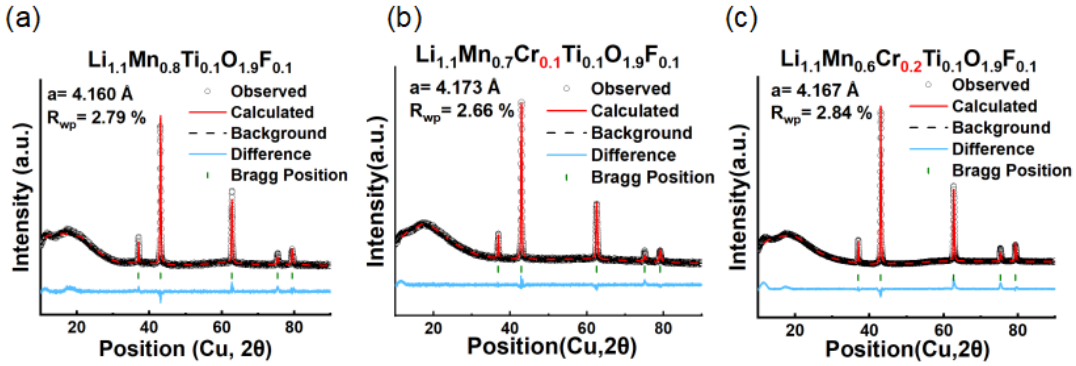

Figure 4. Rietveld refinements of (a) pristine $Li_{1.1}Mn_{0.8}Ti_{0.1}O_{1.9}F_{0.1}$ (L11M8C0), (b) $Li_{1.1}Mn_{0.7}Cr_{0.1}Ti_{0.1}O_{1.9}F_{0.1}$ (L11M7C1) and (c) $Li_{1.1}Mn_{0.6}Cr_{0.2}Ti_{0.1}O_{1.9}F_{0.1}$ (L11M6C2).

Scanning Electron Microscope: The scanning electron microscope (SEM) images and corresponding energy-dispersive X-ray spectroscopy (EDS) element maps in Figure 5 show that all elements are homogeneously distributed in all three pristine samples. The particle sizes are all around 5 μm.

(a)

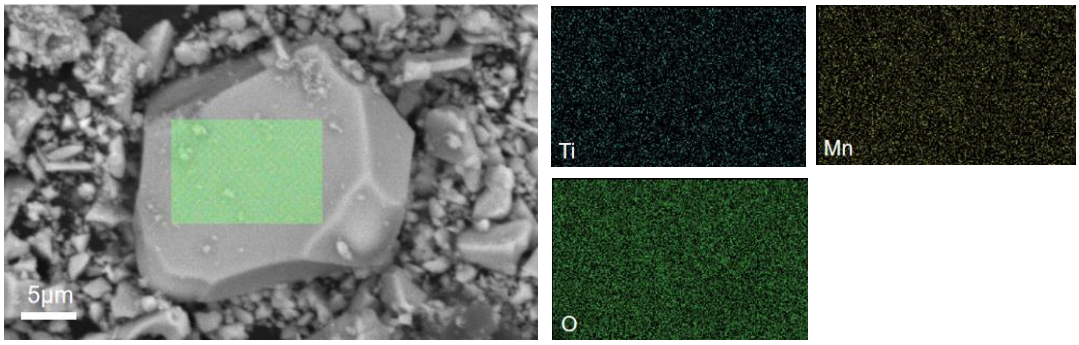

(b)

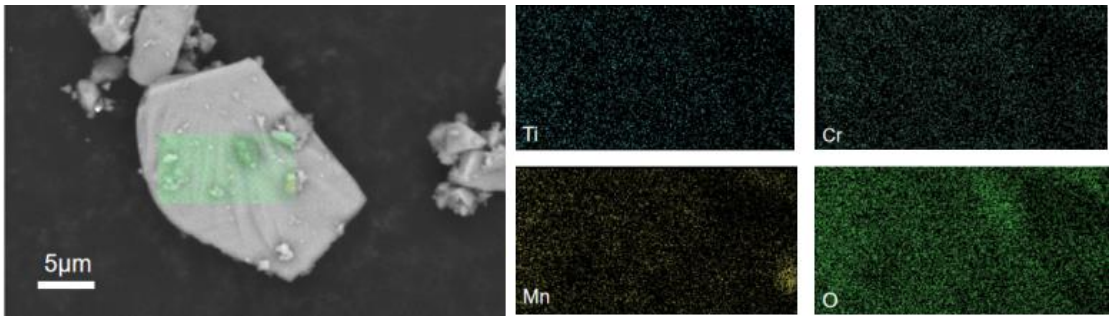

(c)

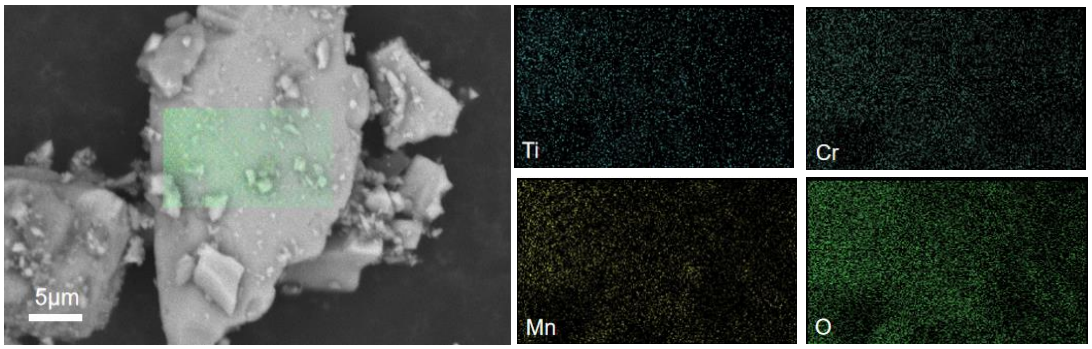

Figure 5. SEM and EDS images of (a) L11M8C0, (b) L11M7C1 and (c) L11M6C2 particles.

Results

1. Delithiation and heating promote the transformation

To promote the transformation, we delithiated cathodes electrochemically to create vacancy and heated cathodes in the box furnace at 150 °C for 30 minutes to provide energy for cation migration, especially for Mn ions. The three different delithiation levels studied were L11M8C0 with delithation level of 0.3 Li/f.u., 0.5 Li/f.u., and 0.7 Li/f.u., respectively. L11M8C0 was measured as the baseline.

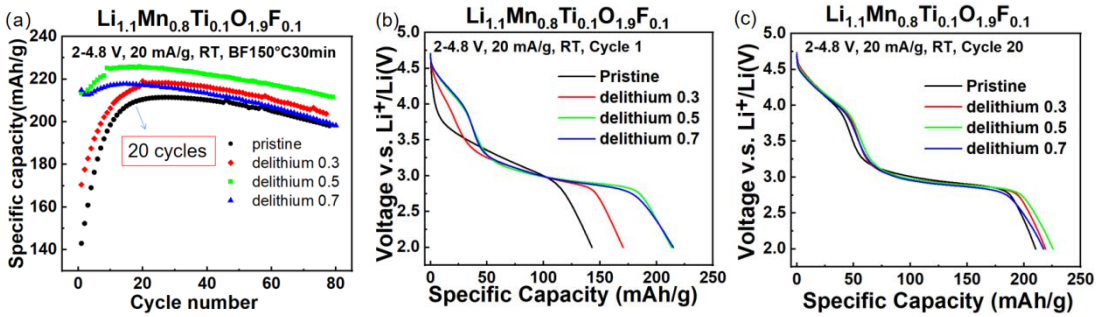

Figure 6. The voltage profiles of pristine and the pristine after delithiation level of 0.3, 0.5, and 0.7 Li/f.u. followed by heating at 150 °C for 30 minutes. (a) Capacity retention over 100 cycles of L11M8C0. (b) Voltage profiles during the first cycle of L11M8C0 and that after delithiation. (c) Voltage profiles during the 20th cycle of L11M8C0 and that after delithiation. The samples were cycled between 2- 4.8 V at 20mA/g.

In Figure 6a, the capacity of L11M8C0 reaches maximum at the 20th cycle, while samples with delithiation level of 0.3, 0.5 and 0.7 Li/f.u. reach the maximum capacities at the 20th, 10th, 15th cycle respectively. Figure 6b shows that after delithiation, the

voltage profile for first cycle during discharge shows plateau-like feature near 4 V and 3 V regions, and delithiation 0.5 and delithiation 0.7 samples show more apparent features, which would only appear after several electrochemical cycles. Figure 6c presents the voltage profiles of the 20th cycle, which show that all the samples have a similar plateau-like feature near 4 V and a plateau near 3 V. Also, the capacity of cathodes after delithiation are larger than that of pristine.

In conclusion, the more apparent spinel-like feature in the first cycle after delithiation and heating prove that such strategy accelerate the transformation, and the voltage profiles of the 20th cycle shows the strategy increases the capacity.

2. Cr ions hinder the transformation from DRX to Delta.

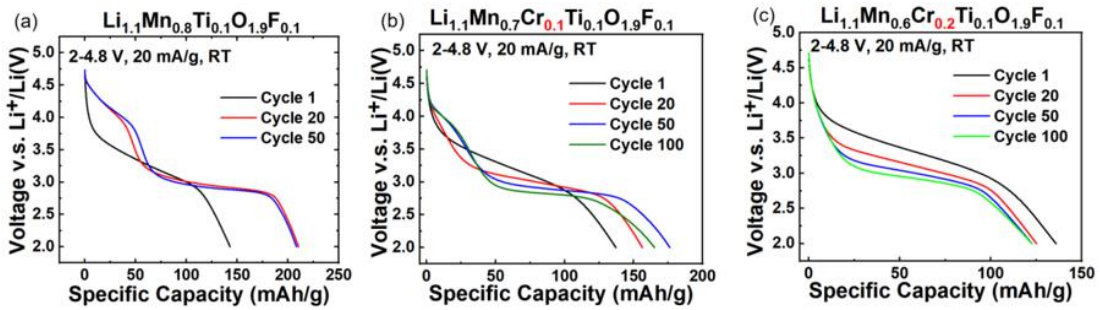

Figure 7. The voltage profile of (a) L11M8C0 (b) L11M7C1 (c) L11M6C2 . The samples were cycled between 2- 4.8 V at 20 mA/g.

To investigate the effect of Cr in the transformation from DRX to Delta, we measured the voltage profiles of L11M8C0, L11M7C1 and L11M6C2. For L11M8C0 (Figure 7a), the plateaus around 4 V and 3V become apparent after 20 cycles. In the first 20 cycles, the capacity increases continuously, reaching the maximum 210 mAh/g at the 20th cycle, and then the capacity decreases, indicating the transformation from DRX to Delta has finished. However, for Li11M7C1 (Figure 7b), the plateau-like feature near 4 V does not appear until the 50th cycles. The capacity increases with its maximum capacity 176 mAh/g appearing at the 50th cycle. The phenomenon that the plateau-like feature appears later than L11M8C0 indicates Cr hinders the transformation from DRX to Delta, while the lower capacity indicates the negative effect of Cr in capacity. Differently, L11M6C2 (Figure 7c) does not show any plateau-like feature near 4 V or 3 V after 100 cycles, and its capacity gradually decreases, indicating that L11M6C2 does not transform to Delta under the cycling condition. Comparing the three voltage profiles, we can conclude that doping Cr hinders the transformation and decreases the capacity. The voltages profiles indicate that most of Cr ions are in the valence of 3+ during

cycling, occupying octahedral sites and hinder the migration of Li ions, which lower the capacity.

3. Optimizing the heating temperature to promote the transformation

We showed that delithiation and heating promote the transformation from DRX to Delta in the previous part, To relieve the negative effect of Cr, we applied the same method to L11M7C1 and L11M6C2 and synthesized $Li_{0.8}Mn_{0.7}Cr_{0.1}Ti_{0.1}O_{1.9}F_{0.1}$ (L8M7C1), $Li_{0.6}Mn_{0.7}Cr_{0.1}Ti_{0.1}O_{1.9}F_{0.1}$ (L6M7C1) $Li_{0.4}Mn_{0.7}Cr_{0.1}Ti_{0.1}O_{1.9}F_{0.1}$ (L4M7C1), $Li_{0.6}Mn_{0.6}Cr_{0.2}Ti_{0.1}O_{1.9}F_{0.1}$ (L6M6C2) and $Li_{0.4}Mn_{0.6}Cr_{0.2}Ti_{0.1}O_{1.9}F_{0.1}$ (L4M6C2). After delithiation, we heated cathodes at 150 °C for 30 minutes and then cycling them.

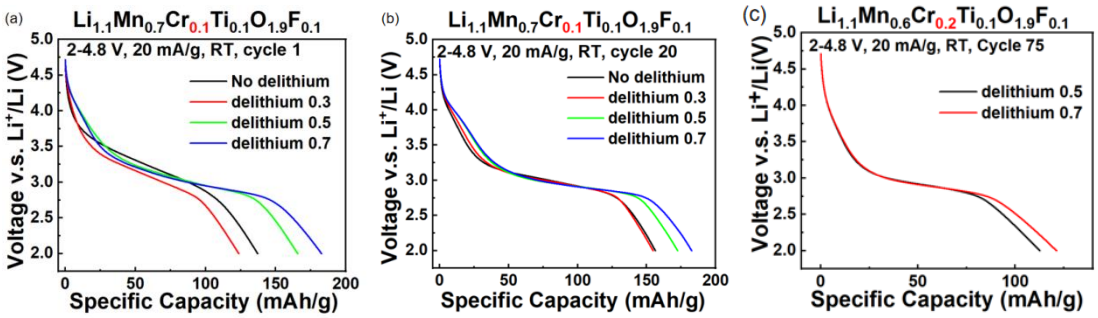

Figure 8. (a) The voltage profiles of the first cycle of L11M7C1, L8M7C1, L6M7C1 and L4M7C1. (b) The voltage profiles of the 20th cycle of L11M7C1, L8M7C1, L6M7C1 and L4M7C1 followed by hearing at 150 C for 30 minutes. (c) The coltage profiles of the 75th cycle of L6M6C2 and L4M6C2. The samples were cycled between 2- 4.8 V at 20mA/g.

Figure 8a and Figure 8b show that after delithiaiton level of 0.7 Li/f.u. and heating at 150 °C for 30 minutes, L4M7C1 demonstrates the most apparent spinel-like feature. Since Cr hinders the transformation, the capacity is still less than that of pristine L11M8C0. Figure 8c shows L11M6C2 can not form Delta with delithiation level of 0.5 and 0.7 Li/f.u. and heating at 150 °C for 30 minutes after 75 cycles, indicating heating at 150 °C can not relieve the negative effect of Cr. Having realized Cr hinders the transformation from the voltage profiles, we elevated the heating temperature to 250 °C to accelerate the migration of cations.

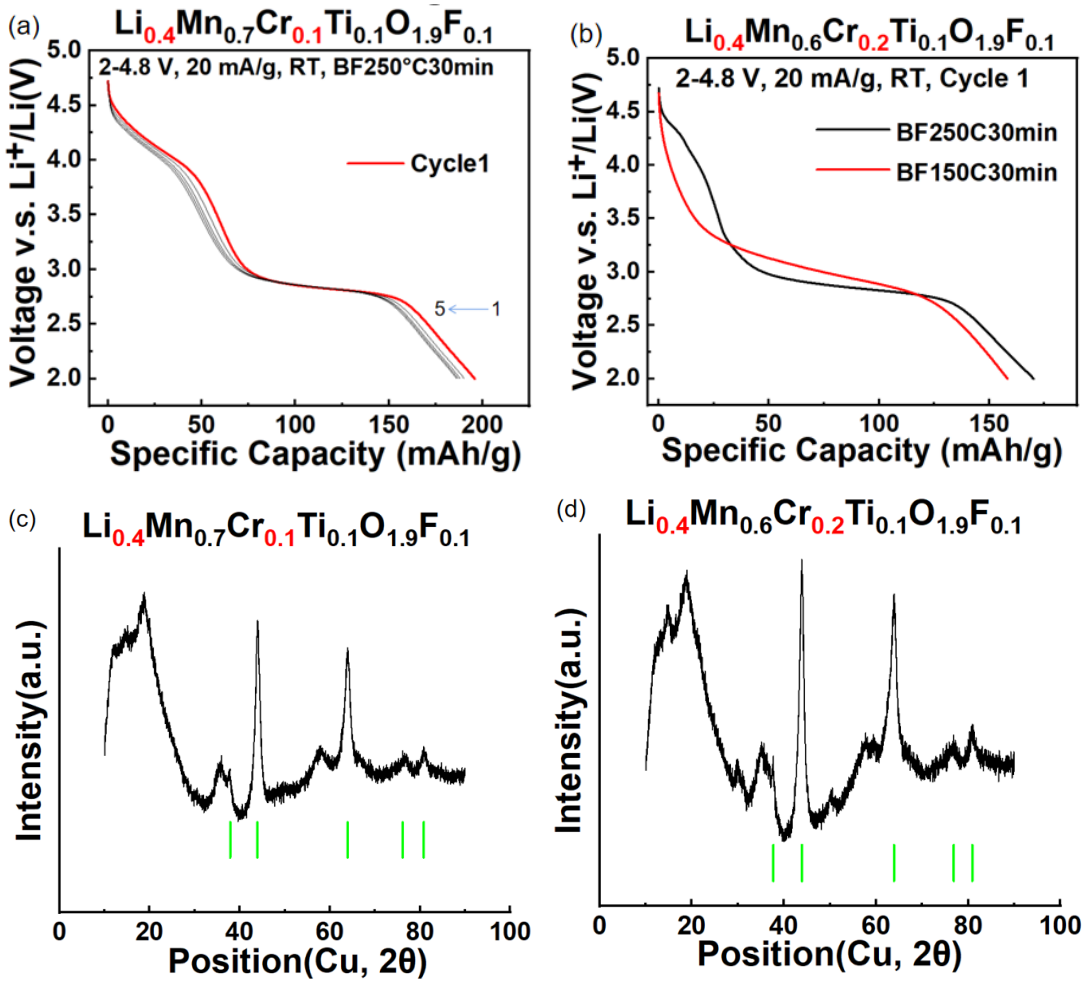

Figure 9. (a) The voltage profiles of the initial five cycles of L4M7C1 after heating at 250 °C for 30 minutes. (b) The voltage profile of the first cycle of L4M6C2 after heating at 150 °C and 250 °C for 30 minutes. The cathodes were measured between 2- 4.8 V at 20 mA/g. (c)(d) The XRD of L4M7C1 and L4M6C2 with PVDF binder. The green lines represent Bragg diffraction peaks of DRX while the star signs represent Bragg diffraction peaks of spinel-like structure.

After delithiation of 0.7 Li/f.u. and heating at 250 °C for 30 minutes, both L4M7C1 and L4M6C2 show spinel-like feature in the first cycle (Figure 9a, 9b). In Figure 9a, the voltage profile of L4M7C1 shows an apparent plateau-like feature near 4 V and 3 V , and the capacity continuously decreases after the first cycle, with a maximum specific capacity of 196 mAh/g, which is much larger than that of the cathode heated at 150 °C, indicating the transformation from DRX to Delta has completed. Figure 9b compares the voltage profiles of the first cycle of L4M7C1 after heating at 150 °C and 250 °C for 30 minutes, from which we can clearly observe the spinel-like features when heating at 250 °C. From the ex-situ XRD using PVDF binder, the peaks marked by star in Figure 9c and 9d can be indexed to spinel peak, and the DRX peaks, marked by green

line, also indicate that the anion lattice remain its long-range ordering after transformation.From both electrochemical and XRD results, we can conclude that Delta can be synthesized successfully without long-time electrochemical cycles.

We further conducted in-situ XRD (Figure 10), which shows no detrimental two-phase reaction around 2.75 V during the first discharge.

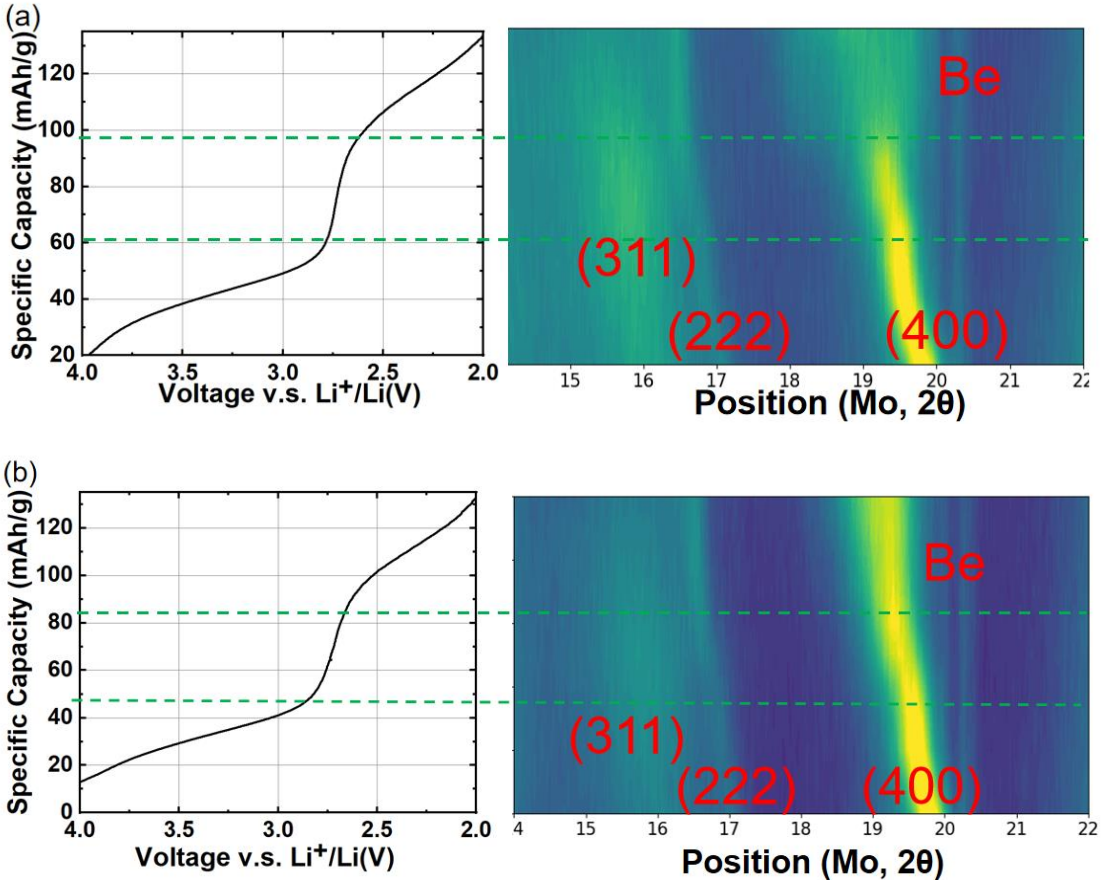

Figure 10. The voltage profile of the first discharge process of (a) L4M7C1 and (b) L4M6C2, and the corresponding in-situ X-ray diffraction patterns. The samples were cycled between 2- 4.8 V at 20mA/g.

However, higher heating temperature does not always lead to better performance. When we heat the to the pristine sample L11M8C0 at 250 °C, aiming to form Delta in the first cycle. From the electrochemical data in Figure 11a, we can conclude higher temperature does not increase the capacity or result in more apparent spinel-like features in L4M8C0. After delithiation level of 0.7 Li/f.u. and heating at 150 °C, pristine sample still requires 15 cycles to finish the transformation. Although heating at 200°C leads to a lower capacity in the first cycle, Figure 11b shows the capacity decreases from cycle 1 to cycle 5, indicating the transformation finishes after heating at 200 °C for 30 minutes. We think the optimized temperature for the pristine sample is between

150 °C and 200 °C, where it can get its maximum capacity and complete the transformation.

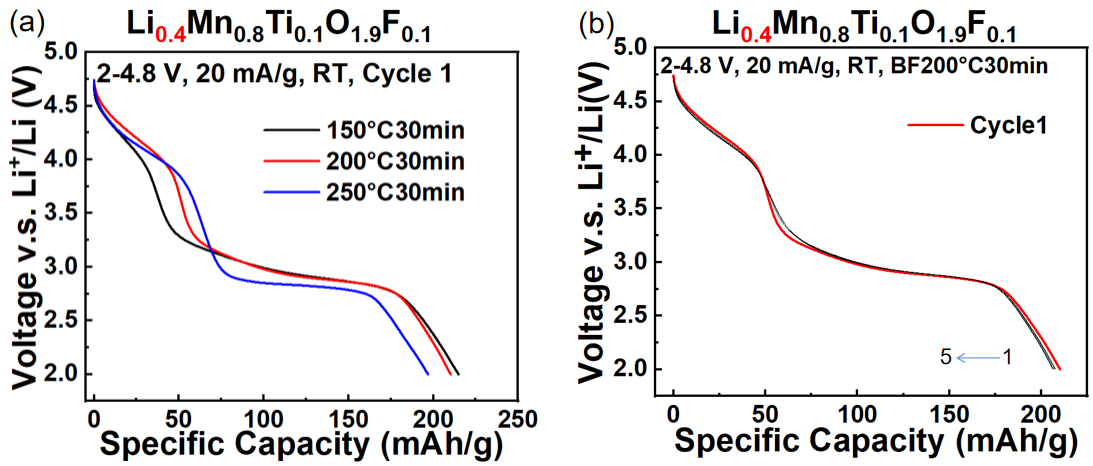

Figure 11. (a) The voltage profiles of the furst cycke of L4M8C0, which is heated at 150 °C, 200 °C and 250 °C for 30 minutes. (b) The initial five cycles of L4M8C0, which is heated at 200 °C for 30 minutes. The samples were cycled between 2- 4.8 V at 20mA/g.

4. L4M7C1 performs worse at high rate compared with L4M8C0 .

L4M8C0 and L4M7C1 were tested under higher rates of 100mA/g, 200mA/g and 1A/g. Both cathodes were heated at 250°C for 30 minutes, which was the optimum condition of L4M7C1 instead of L4M8C0. However, L4M7C1 still demonstrates worse capacity than L4M8C0, indicating doping Cr decreases capacity. For L4M8C0 and L4M7C1, galvanostatic cycling at 20 mA/g between 2-4.8 V after delithiation level of 0.7 Li/f.u. and heating at 250 °C for 30 minutes deliver initial specific discharge capacity of 197 mAh/g and 196 mAh/g respectively (Figure 9a, 9b). Upon increasing the current density from 20 to 1000 mA/g, the initial discharge capacity are reduced to 81 mAh/g and 58 mAh/g, indicating the strategy of doing Cr does not improve the rate performance.

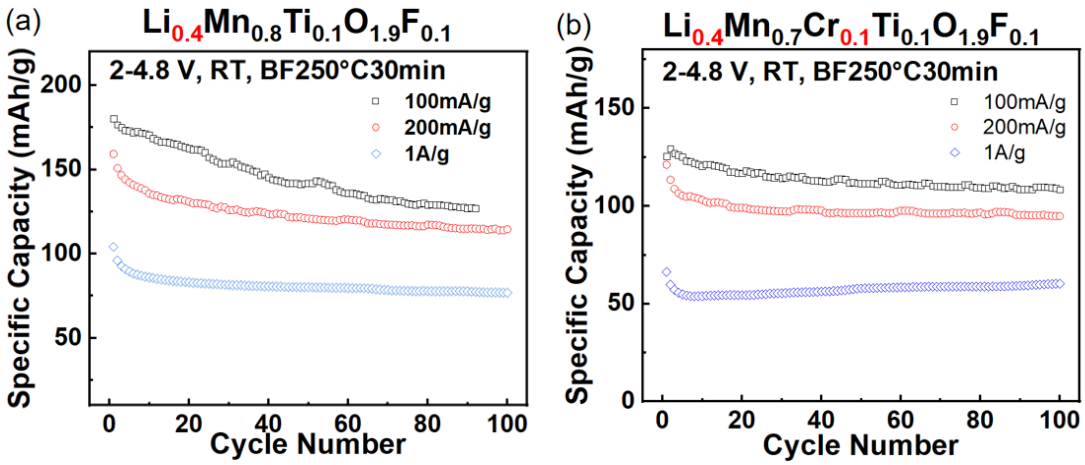

Figure 12. The rate performance of L4M8C0 (a) and L4M7C1 (b). The samples were measured between 2- 4.8 V at rate 100mA/g, 200mA/g and 1A/g.

Discussion

1. Optimum temperature

From the experiment, we can define an optimum temperature for each sample. to be the temperature that can lead to complete Delta transformation after delithiation level of 0.7 Li/f.u.. For example, the optimum temperature of L4M7C1 is approximately 250°C, proved by Figure 9a. Optimum temperatures of those three cathodes are shown in Table 1. We did not test the optimum temperature of L4M6C2 because we used PTFE as the binder, whose melting point was 327°C.

Table 1. The optimum temperatures of three cathodes

Cathode	Optimum temperature
$Li_{0.4}Mn_{0.8}Ti_{0.1}O_{1.9}F_{0.1}$	approximately 200°C (slightly lower)
$Li_{0.4}Mn_{0.7}Cr_{0.1}Ti_{0.1}O_{1.9}F_{0.1}$	approximately 250°C
$Li_{0.4}Mn_{0.6}Cr_{0.2}Ti_{0.1}O_{1.9}F_{0.1}$	Higher than 250°C

2. The effect of doping Cr

Comparing the pristine and samples doped with Cr, we conclude that Cr hinders

the transformation from DRX to Delta. Theoretically, the process from DRX to Delta is actually from fully disordered to partially ordered cathode. In other words, entropy decreases during the process. However, entropy increases when doping Cr in DRX, which is contrary to our aim. In this perspective, there is no wonder that Cr hinders the transformation.

More convincing, from the XAS results in Figure 13, L4M7C1 at different state of charge is shown .

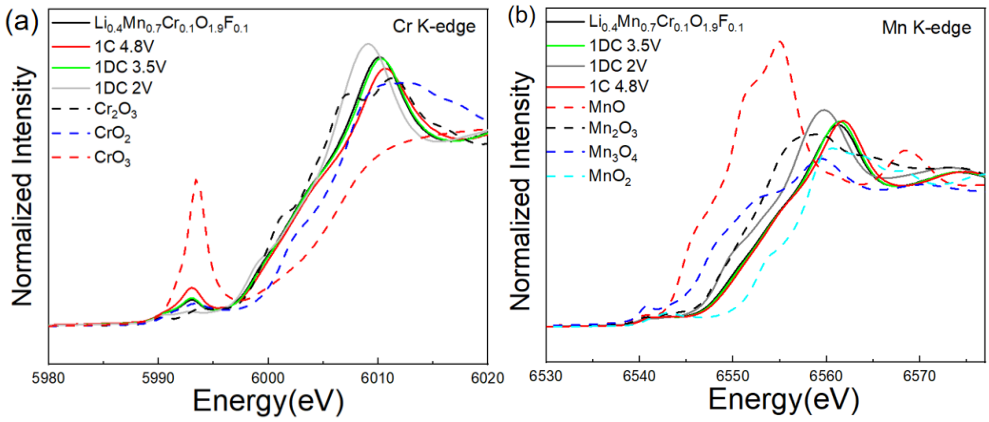

Figure 13. (a) Cr K-edge XANES spectra of L4M7C1. The Cr_2O_3, CrO_2, CrO_3 standards spectra are plotted as dashed lines. (b) Mn K-edge XANES spectra of L4M7C1. The MnO, Mn_2O_3, MnO_2, Mn_3O_4 standards spectra are plotted as dashed lines.

A prominent pre-edge component in the Cr K-edge XANES is a characteristic feature of Cr^{6+}, which is attributed to the 1s→3d transition[11]. Comparison of the pre-edge intensities in the Cr K-edge XANES spectra of the CrO_3 standard and the 1C 4.8 V provides strong evidence that most of Cr^{3+} ions in L4M7C1 are not oxidized to Cr^{6+} ions (Figure 13a). So even at 4.8 V, most of Cr ions take up octahedral sites, hindering the migration of Li ions. Mn K-edge XANES (Figure 13b) shows the valence of Mn ions during cycling, which confirms Mn +3 to +4 redox is mainly utilized when cycling between 2-4.8 V.

To take advantage of Cr ions in the transformation form DRX to Delta, other methods are needed to oxidize Cr^{3+} ions. So we extended the voltage window to 2-5 V (Figure 14). However, the voltage profile does not show much improvement, indicating Cr^{3+} ions are not oxidized to Cr^{6+} even at 5 V.

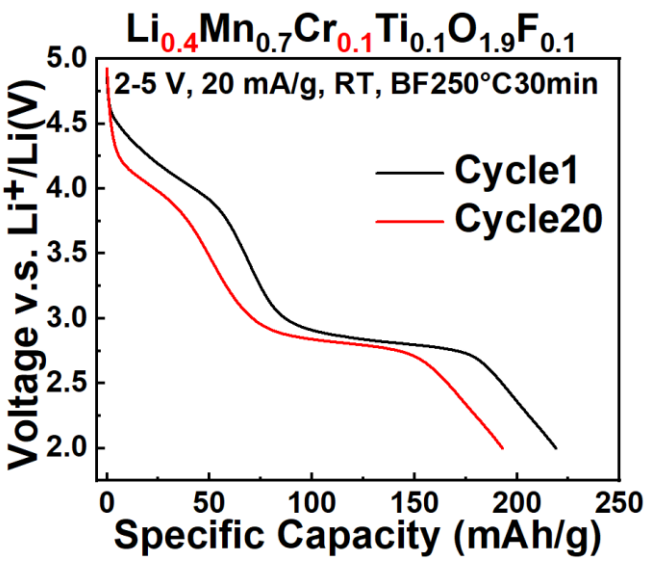

Figure 14. The voltage profiles of L4M7C1 after heating at 250 °C for 30 minutes. The samples were cycled between 2- 5 V at 20mA/g.

Conclusion

Through electrochemical test, ex-situ XRD, and in-situ XRD, we proved that L11M7C1 and L11M6C2 can be transformed to Delta with delithiation level of 0.7 Li/f.u. and heating at 250 °C for 30 minutes, and two-phase reaction did not occur during electrochemical cycling, which is advantageous over ordered spinel. Further, delithiation and heating promote the transformation, and optimum temperatures are estimated in the experiment, which can provide guidelines toward future synthesis. However, Cr was found to hinder the transformation since most of the Cr ions cannot be oxidized to Cr^{6+} and occupy the octahedral sites upon charging to 4.8 V. Instead, Cr in tetrahedral sites hindering the migration of Li ions, shown in XAS images. After being doped with Cr, cathodes not only had a lower capacity, but also performed worse in high-rate testing circumstance. To take full advantage of Cr ions, other methods are needed to oxidize Cr^{3+} to Cr^{6+} during cycling, maybe Cr^{6+} ions can be added directly when synthesizing cathodes. In the future, transmission electron microscopy (TEM) and scanning transmission electron microscopy (STEM) can be applied to confirm Delta structure more directly. Solid-state nuclear magnetic spectroscopy (ssNMR) can be applied to probe the evolution of Li local environment upon cycling. Resonant inelastic X-ray scattering (RIXS) can be applied to figure out oxygen redox process. First-principles density functional theory (DFT) calculations can be performed to obtain an accurate description of the structural energies and oxidation states of different cathode materials.

Reference

1. A. Urban , J. Lee and G. Ceder , The configurational space of rocksalt-type oxides for high-capacity lithium battery electrodes, *Adv. Energy Mater*., 2014, 4 , 1400478.

2. Olivetti, E. A., Ceder, G., Gaustad, G. G. & Fu, X. Lithium-ion battery supply chain considerations: analysis of potential bottlenecks in critical metals. *Joule1*, 229–243 (2017).

3. R. J. Clément , Z. Lun and G. Ceder , Cation-disordered rocksalt transition metal oxides and oxyfluorides for high energy lithium-ion cathodes, Energy Environ. Sci., 2020, 13 , 345.

4. J. Lee, A. Urban, X. Li, D. Su, G. Hautier, G. Ceder, Unlocking the Potential of Cathode-Disordered Oxides for Rechargeable Batteries, *Science*. 343 (2014) 519-522.

5. Lun, Z., Ouyang, B., Kwon, DH. et al. Cation-disordered rocksalt-type high-entropy cathodes for Li-ion batteries. *Nat. Mater*. 20, 214–221 (2021).

6. Cai, Z.; Zhang, Y. Q.; Lun, Z.; Ouyang, B.; Gallington, L. C.; Sun, Y.; Hau, H. M.; Chen, Y.; Scott, M. C.; Ceder, G. Thermodynamically driven synthetic optimization for cation-disordered rock salt cathodes. *Adv. Energy Mater*. 2022, 12, 2103923.

7. Li, L., Lun, Z., Chen, D., Yue, Y., Tong, W., Chen, G., Ceder, G., and Wang, C., Fluorination-enhanced surface stability of cation disordered rocksalt cathodes for Li-ion batteries, *Adv. Funct. Mater*., 2021, vol. 31, no. 2101888.

8. Ji, H., Wu, J., Cai, Z. et al. Ultrahigh power and energy density in partially ordered lithium-ion cathode materials. *Nat Energy.* 5, 213–221 (2020).

9. Huang, Y.; Dong, Y.; Li, S.; Lee, J.; Wang, C.; Zhu, Z.; Xue, W.; Li, Y.; Li, J. Lithium Manganese Spinel Cathodes for Lithium-Ion Batteries. *Adv. Energy Mater*. 2021, 11, 2000997.

10. Cai,Z., Ji, H. et al., Realizing continuous cation order-to-disorder tuning in a class of high-energy spinel-type Li-ion cathodes, *Matter*. 2021.10.013.

11. Huang, J., Zhong, P., Ha, Y. et al. Non-topotactic reactions enable high rate capability in Li-rich cathode materials. *Nat Energy* 6, 706–714 (2021).

荣誉证书

陈祥雨同志：

您指导的本科毕业设计（论文）《可见光诱导的碳－磷键构建》，获评为2024年北京市普通高校优秀本科毕业设计（论文），您获评为优秀指导教师。

特发此证，以资鼓励。

北京市教育委员会

2024年11月

荣誉证书

廖鹏崴同学：

您的本科毕业设计（论文）《可见光诱导的碳-磷键构建》，获评为2024年北京市普通高校优秀本科毕业设计（论文）。

特发此证，以资鼓励。

北京市教育委员会

2024年11月

OL Organic Letters

pubs.acs.org/OrgLett Letter

N-Heterocyclic Nitrenium-Catalyzed Photohomolysis of CF_3SO_2Cl for Alkene Trifluoromethylation

Xiao-Jian Ren,[§] Peng-Wei Liao,[§] He Sheng,[§] Zhi-Xiang Wang,* and Xiang-Yu Chen*

Cite This: *Org. Lett.* 2023, 25, 6189–6194 Read Online

ACCESS | Metrics & More | Article Recommendations | Supporting Information

ABSTRACT: N-Heterocyclic nitreniums (NHNs) have been utilized as Lewis acid catalysts to activate substrates with lone pairs. Alternative to their conventional applications, we have discovered that NHNs can also serve as charge transfer complex catalysts. Herein, we present another potential of NHNs by utilizing a weak interaction between NHNs and CF_3SO_2Cl. The method promotes CF_3SO_2Cl to undergo photohomolysis, resulting in the CF_3 radical. Mechanistic studies suggested that the weak interaction could be due to the π-hole effect of NHNs.

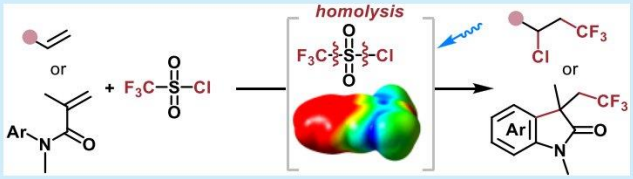

Downloaded via UNIV OF CHINESE ACADEMY OF SCIENCES on September 6, 2023 at 11:52:47 (UTC).
See https://pubs.acs.org/sharingguidelines for options on how to legitimately share published articles.

N-Heterocyclic nitreniums (NHNs), which are isoelectronic and isostructural counterparts of N-heterocyclic carbenes, have gained increasing interest in recent times due to their easy accessibility, cost-effectiveness, and stability.[1] A recent development in this area was the utilization of NHNs as Lewis acid catalysts for activating substrates with lone pair donors, as demonstrated by the research groups of Mehta, Goicoechea,[2] Gandelman,[3] and García Mancheño[4] (Figure 1A). Despite the success of these ionic transformations, the catalytic potential of NHNs in radical reactions remains relatively underdeveloped. In recent discoveries, we found that NHNs can be employed as charge transfer complex (CTC) catalysts in the presence of tetramethylethylenediamine (TMEDA) for the single electron reduction of carbon–halogen bonds. In this system, NHNs act as organocatalytic electron acceptors, while the counterion I^- and/or TMEDA serves as catalytic electron donors (Figure 1B).[5] This finding demonstrates that the NHN iodide salt is an excellent candidate for CTC catalysis. As part of our ongoing research in weak interaction-enabled photoreactions,[6] we set out to explore the possibility of developing new catalytic abilities of NHNs through the utilization of weak interactions.

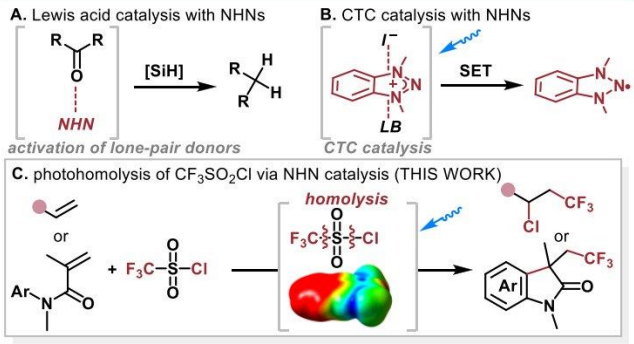

Figure 1. Catalytic activities of NHNs.

Recently, the application of pnictogen compounds' sigma (σ)–hole interaction has been actively studied as a promising tool in synthetic chemistry.[7] In this context, remarkable progress has been achieved in the realm of antimony catalysis by research groups of Gabbaï,[8] Matile,[9] and Tan.[10] However, the potential of weak interactions between N-containing compounds remains largely unexplored. This is primarily due to the scarcity of σ-holes in the nitrogen atoms. On the other hand, there is another type of π-hole interaction, where an electropositive region located perpendicularly above the molecular framework acts as the Lewis acid center.[11] Hence, we envisioned that the π-hole effect of NHNs could be utilized to activate organic halides under light irradiation. If feasible, it would unlock new capabilities of NHNs and new approaches for generating alkyl radicals.

The trifluoromethyl group holds great significance in pharmaceutical chemistry due to its advantageous properties, such as high-fat solubility, excellent metabolic stability, high electronegativity, and good bioavailability.[12] Recently, there has been extensive development in photocatalytic trifluoromethylation, providing a powerful means of introducing the trifluoromethyl group into alkenes. In this regard, trifluoromethanesulfonyl chloride (CF_3SO_2Cl) has emerged as a valuable, effective, and cost-efficient reagent for trifluoromethylation.[13] Herein, we showed that readily available NHNs can establish a weak interaction with CF_3SO_2Cl, enabling the

Received: July 20, 2023
Published: August 14, 2023

ACS Publications © 2023 American Chemical Society

https://doi.org/10.1021/acs.orglett.3c02380
Org. Lett. 2023, 25, 6189–6194

photohomolysis of CF_3SO_2Cl for the generation of the CF_3 radical. This activation mechanism differs from the previous approach involving single-electron-transfer processes (Figure 1C).

Our investigation began with the reaction between allyl benzoate **1** and CF_3SO_2Cl (Table 1). To our delight, we obtained the desired product **2** with an 80% yield when employing 1 mol % of NHN **A1** as the catalyst without any additive in CH_3CN under blue light irradiation (entry 1). NHN **A2**, which has a BF_4^- counterion instead of OTf^-, resulted in a slightly decreased yield (entry 2). When NHN **A1** was replaced with either NHN **B** or NHN **C**, no reaction occurred (entries 3 and 4), because the two NHNs could not form visible light induced photoactive complexes with CF_3SO_2Cl (*vide infra*). Solvent screening showed that CH_3CN was the best choice (entries 5–8). Control experiments confirmed that no reaction was observed in the absence of visible light or NHN **A1** (entries 9 and 10).

Table 1. Optimization of the Reaction Conditions

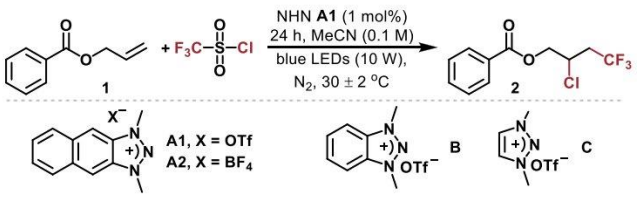

Entry	Variations from standard conditions	Yield (%)[a]
1	none	80 (75)[b]
2	NHN **A2** instead of **A1**	75
3	NHN **B** instead of **A1**	trace
4	NHN **C** instead of **A1**	trace
5	THF	30
6	DMA	50
7	DMF	31
8	C_2H_5OH	30
9	without NHN **A1**	NR
10	without irradiation, 35 °C	NR

[a]Yields were determined by ^{19}F NMR analysis using (trifluoromethyl)benzene as an external standard. [b]The value within parentheses refers to the yield of isolated products.

With the optimized conditions in hand, the reaction scope was then evaluated (Scheme 1). Both electron-donating (4-OMe) and electron-withdrawing (4-CF_3) groups on the phenyl ring were tolerable and provided the desired products **3** and **4** in 65% and 58% yields, respectively. Alkyl substituents afforded the desired products **5** and **6** in good yields. Substrates with various functional groups, including aryl, ether, and amide groups (**7**–**10**), were also tolerated in the reaction without an apparent change in the yield. To demonstrate the synthetic utility of this transformation, the late-stage structural modifications of drug molecules and natural products were then performed. The alkenes derived from various scaffolds gave desired products **11**–**14** in 45–59% yields. In addition, α,β-unsaturated esters could also be applied for the reaction (**15**).

As the oxindole scaffolds are widely used as raw material for spices, dyes, amino acids, and pesticides,[14] a variety of substituted N-arylacrylamides were tested in the presence of K_2HPO_4 as the base (Scheme 2). We were pleased to find that both electron-donating (4-Me and 4-OMe) and electron-withdrawing (4-Br, 4-CO_2Me, 4-CN, and 4-CF_3) groups on the phenyl ring reacted well, giving the corresponding trifluoromethylated products **16**–**22** in 56–85% yields. The ortho-substituents (2-Me, 2-Cl, and 2-Br) also proceeded well (**23**–**25**). After replacement of the methyl group on nitrogen by -Et, -Ph, and a cyclic phenylpropyl group, the reactions were not significantly affected (**26**–**29**). Given the usefulness of the CF_3 and oxindole groups in medicinal chemistry and drug development, we successfully installed them into natural products and pharmaceutical derivatives in moderate yields (**30**–**34**).

To gain insight into the reaction mechanism, we carried out experimental mechanistic studies. The UV–vis spectroscopy experiments in Figure 2A indicated that NHN **A1** is

Scheme 1. Reaction Scope for the Chlorotrifluoromethylation[a]

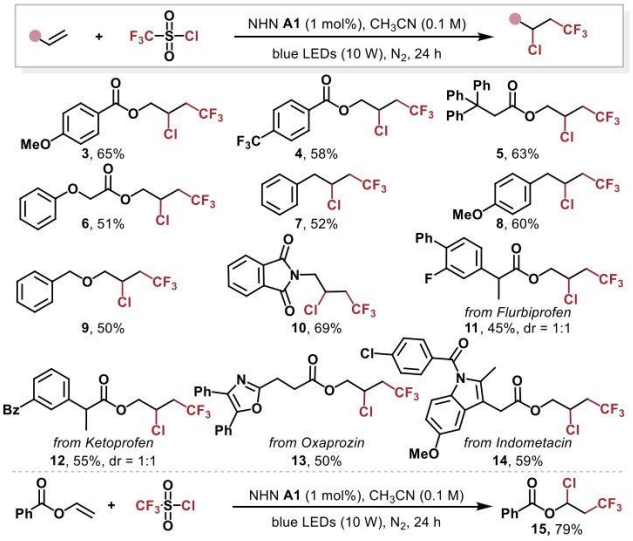

[a]Yield of the isolated products. The dr values were determined by ^1H NMR analysis.

Scheme 2. Reaction Scope for the Synthesis of Oxindoles[a]

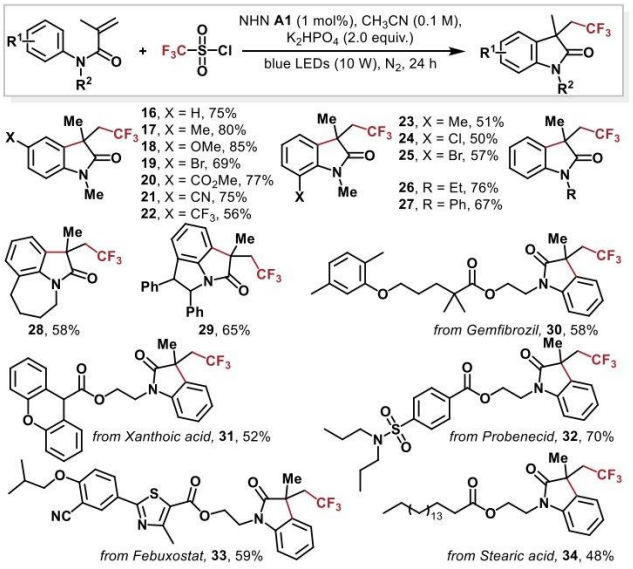

[a]Yield of the isolated products.

https://doi.org/10.1021/acs.orglett.3c02380
Org. Lett. 2023, 25, 6189–6194

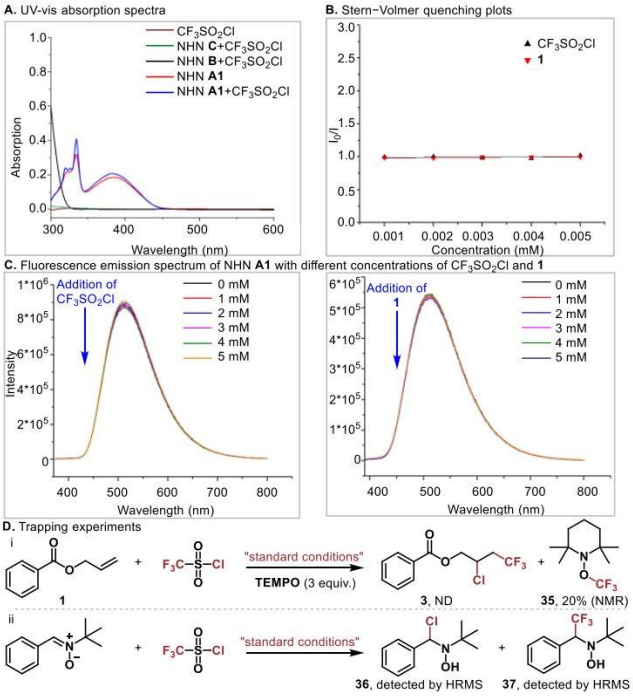

Figure 2. (A) Partial UV−vis absorption spectra of NHN **A1**, NHN **B**, NHN **C**, and CF_3SO_2Cl and the mixtures in CH_3CN (see the Supporting Information for the details). (B) Stern−Volmer quenching plots of NHN **A1** with CF_3SO_2Cl and **1**. (C) Fluorescence emission spectrum of NHN **A1** with different concentrations of CF_3SO_2Cl and **1**. (D) Trapping reactions.

photoactive but CF_3SO_2Cl is not. The addition of CF_3SO_2Cl to NHN **A1** solution marginally enhances the absorption of NHN **A1**, but NHN **A1** itself and the mixture show evident absorption in the visible light region. In contrast, the NHN **B**/CF_3SO_2Cl and NHN **C**/CF_3SO_2Cl mixtures did not exhibit observable absorption in the visible light region; thus, they could not be excited by blue light, explaining why the two NHNs were unable to catalyze the reaction (entries 3 and 4 in Table 1). The Stern−Volmer plots showed that the luminescence of the photoexcited NHN **A1** could not be quenched by either substrate **1** or CF_3SO_2Cl. The experiments implied that the photoactivation of CF_3SO_2Cl could take place without involving electron transfer or energy transfer (Figure 2B and C). Furthermore, TEMPO (2,2,6,6-tetramethylpiperidin-1-oxyl) inhibited the reaction completely, and the CF_3 radical trapping adduct **35** could be obtained in 20% NMR yield ((i) in Figure 2D). The radical trapping experiment (ii) in Figure 2D demonstrated the generation of Cl and CF_3 radicals. The EPR studies clearly revealed the generation of Cl and CF_3 radicals in this system. A solution of CH_3CN, CF_3SO_2Cl, NHN **A1**, and spin trap PBN was monitored by EPR spectroscopy, and no signal was observed without light. Upon blue light irradiation, the spin-trapped Cl and CF_3 radical adducts were immediately formed.[15] The observed EPR spectra of **^{37}Cl-36**, **^{35}Cl-36**, and **37** were successfully simulated based on the calculated coupling constants (Figure S9 in the Supporting Information). In addition, Job's plot and ^{1}H NMR titration experiments indicated that the complexation of NHN **A1** and CF_3SO_2Cl occurred via a 1:1 ratio with an association constant of 2.16 M^{-1} in CH_3CN (Figure S13 in the Supporting Information). Based on these experimental results, we reasoned that the reaction took place via photolysis of CF_3SO_2Cl to generate CF_3 and Cl radicals.

To further understand the photolysis mechanism, density functional theory (DFT) and time-dependent DFT (TDDFT) calculations were performed (see the Supporting Information for the computational details). It was predicted that a minimum energy of 33.2 kcal/mol is required for CF_3SO_2Cl to undergo homolysis. On the other hand, the calculated maximum absorption wavelength of CF_3SO_2Cl is 246 nm (Figure 3A); thus, CF_3SO_2Cl itself could not undergo

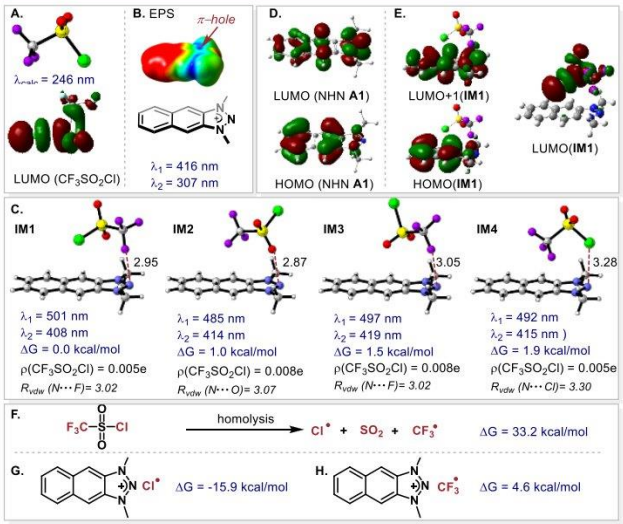

Figure 3. Computational results.

photolysis under blue light irradiation. The electrostatic potential surface (EPS) of NHN **A1** shows an electron-deficient π-hole above the middle nitrogen atom of NHN (Figure 3B). Thus, NHN **A1** and CF_3SO_2Cl could form an ensemble containing various weak bonding complexes, as exemplified by **IM1**−**IM4** (Figure 3C). The occurrence of the weak interaction is indicated by the marked atomic distances, which are shorter or close to the sum of the van der Waals radius of the two atoms. In addition, the CF_3SO_2Cl moiety in these complexes bears positive charges, indicating the electron donation from CF_3SO_2Cl to NHN **A1**. We use **IM1** as an example for the following discussions, which also apply for others.

IM1 features two absorption bands in the visible light region, with wavelengths being λ_1 = 501 and λ_2 = 408 nm, respectively. Comparing the frontier orbitals of NHN **A1** and **IM1** (Figure 3D and E), the λ_2 (408 nm) absorption of **IM1**, mainly due to the HOMO → LUMO+1 electron transition, corresponds to the λ_1 (416 nm) absorption of NHN **A1**, mainly due to the HOMO → LUMO electron transition. The λ_1 absorption of **IM1** mainly originates from the HOMO → LUMO electron transition. Interestingly, the LUMO of **IM1** is nearly the LUMO of CF_3SO_2Cl which features significant characteristics of the S−Cl antibonding orbital. Thus, the photoexcitation of **IM1** at λ_1 would result in the S−Cl bond cleavage, explaining why NHN **A1** can catalyze the homolysis of CF_3SO_2Cl under visible light radiation. The frontier orbitals of **IM2**−**IM4** are displayed in Figure S14, which have characteristics similar to those of **IM1**.

In contrast to NHN **A1**, the complexes formed between NHN **B**/NHN **C** and CF_3SO_2Cl have maximum absorption

https://doi.org/10.1021/acs.orglett.3c02380
Org. Lett. 2023, 25, 6189−6194

wavelengths (351/253 nm, Figure S15 in the Supporting Information) much shorter than that of NHN **A1**, in agreement with the fact that NHN **B**/NHN **C** and CF_3SO_2Cl are not photoactive. Comparing the structures of NHNs **A**−**C** (Table 1), the contrast difference in their photoactivities could be attributed to the greater π conjugation effect in NHN **A** than in NHNs **B** and **C**. In addition, NHN **A1** can further stabilize the Cl radical to favor the photolysis (Figure 3F−H). We attempted to characterize the photolysis pathway by locating an intermediate state in the first excited state. While the geometric optimizations repeatedly failed to deliver a converged structure, we observed that the optimizations tended to fragment CF_3SO_2Cl, giving SO_2 and Cl and CF_3 radicals. We attribute the interaction between NHN **A1** and CF_3SO_2Cl to electron donation from the latter to the former. Alternatively, the in-plane lone pair of NHN **A1** may serve as an electron donor to form a halogen bond with CF_3SO_2Cl. However, attempts to locate such a structure with chlorine of CF_3SO_2Cl pointing to the in-plane lone pair of NHN **A1** tended to give a structure similar to **IM4** (see Figure S16).

According to the above results and previous studies in weak interactions,[16] Figure 4 sketches a possible mechanism for the

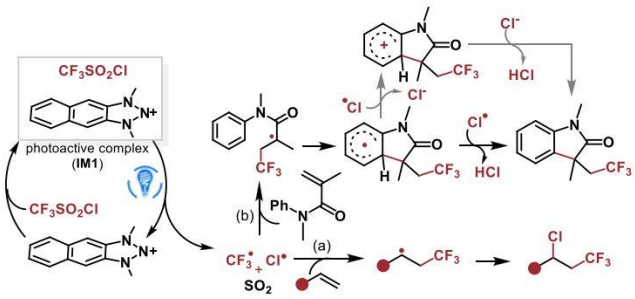

Figure 4. Proposed mechanism.

reactions. The *in situ* formed complex **IM1** is first excited under blue light irradiation, promoting the homolysis of CF_3SO_2Cl to generate Cl and CF_3 radicals, while releasing SO_2. The subsequent reactions may proceed via two possible pathways depending on the substrates. Pathway (a) leads to the products in Scheme 1, where CF_3 and Cl radicals sequentially add to the alkene. Pathway (b) describes the reactions leading to oxindoles. The pathway involves intramolecular cyclization and hydrogen abstraction with the Cl radical. Alternative to the hydrogen atom abstraction involved in pathway (b), the process could also proceed via SET between Cl radical and CF_3 addition radical, followed by deprotonation with Cl^-. Note that the byproduct HCl involved in pathway (b) can be stabilized by the additive K_2HPO_4.

With the mechanism, we tentatively explain the significant yield drops in other solvents, such as DMA and THF. DFT calculations detailed in the Supporting Information showed that the photoactive complexes in these solvents could not be formed as effectively as in CH_3CN, thus decreasing the efficiency of the reaction (see Figure S17). It should be noted that the DFT results point to the occurrence of weak π-hole interaction between NHNs and CF_3SO_2Cl in the ground state. We could not rule out the possibility that the interaction between an excited state of NHN and CF_3SO_2Cl results in the photohomolysis of CF_3SO_2Cl.

In conclusion, the NHN-catalyzed photohomolysis of CF_3SO_2Cl for the generation of the CF_3 radical for trifluoromethylation of alkenes has been developed. The strategy is operationally simple and without using transition metals and oxidants. Mechanistic experiments including NMR titration and Ka determination suggested that the π-hole-enabled weak interaction between NHNs and CF_3SO_2Cl could play a role in enabling the photohomolysis of CF_3SO_2Cl. This method provides a new option for the generation of trifluoromethyl radical.

■ ASSOCIATED CONTENT

Data Availability Statement

The data underlying this study are available in the published article and its Supporting Information.

Supporting Information

The Supporting Information is available free of charge at https://pubs.acs.org/doi/10.1021/acs.orglett.3c02380.

Experimental details, characterization data, DFT studies, and spectra (PDF)

■ AUTHOR INFORMATION

Corresponding Authors

Zhi-Xiang Wang − *School of Chemical Sciences, University of Chinese Academy of Sciences, Beijing 100049, China; Binzhou Institute of Technology, Weiqiao-UCAS Science and Technology Park, Binzhou, Shandong Province 256606, China;* orcid.org/0000-0001-5815-3032; Email: zxwang@ucas.ac.cn

Xiang-Yu Chen − *School of Chemical Sciences, University of Chinese Academy of Sciences, Beijing 100049, China; Binzhou Institute of Technology, Weiqiao-UCAS Science and Technology Park, Binzhou, Shandong Province 256606, China;* orcid.org/0000-0002-0383-0910; Email: chenxiangyu20@ucas.ac.cn

Authors

Xiao-Jian Ren − *School of Chemical Sciences, University of Chinese Academy of Sciences, Beijing 100049, China*

Peng-Wei Liao − *School of Chemical Sciences, University of Chinese Academy of Sciences, Beijing 100049, China*

He Sheng − *School of Chemical Sciences, University of Chinese Academy of Sciences, Beijing 100049, China*

Complete contact information is available at: https://pubs.acs.org/10.1021/acs.orglett.3c02380

Author Contributions

§X.-J.R., P.-W.L., H.S.: These authors contributed equally.

Notes

The authors declare no competing financial interest.

■ ACKNOWLEDGMENTS

Supported by the National Natural Science Foundation of China (22173103 and 22001248) and the Fundamental Research Funds for the Central Universities and the University of the Chinese Academy of Sciences.

■ REFERENCES

(1) (a) Tulchinsky, Y.; Iron, M. A.; Botoshansky, M.; Gandelman, M. Nitrenium ions as ligands for transition metals. *Nat. Chem.* **2011**, 3, 525−531. (b) Tulchinsky, Y.; Kozuch, S.; Saha, P.; Botoshansky, M.; Shimon, L. J. W.; Gandelman, M. Cation−cation bonding in

nitrenium metal complexes. *Chem. Sci.* **2014**, *5*, 1305−1311. (c) Tulchinsky, Y.; Kozuch, S.; Saha, P.; Mauda, A.; Nisnevich, G.; Botoshansky, M.; Shimon, L. J. W.; Gandelman, M. Coordination Chemistry of N-Heterocyclic Nitrenium-Based Ligands. *Chem. -Eur. J.* **2015**, *21*, 7099−7110. (d) Pogoreltsev, A.; Tulchinsky, Y.; Fridman, N.; Gandelman, M. Nitrogen Lewis Acids. *J. Am. Chem. Soc.* **2017**, *139*, 4062−4067. (e) Zhou, J.; Liu, L. L.; Cao, L. L.; Stephan, D. W. Nitrogen-Based Lewis Acids: Synthesis and Reactivity of a Cyclic (Alkyl)(Amino)Nitrenium Cation. *Angew. Chem., Int. Ed.* **2018**, *57*, 3322−3326. (f) Avigdori, I.; Pogoreltsev, A.; Kaushanski, A.; Fridman, N.; Gandelman, M. Frustrated Lewis Pairs Comprising Nitrogen Lewis Acids for Si−H Bond Activation. *Angew. Chem., Int. Ed.* **2020**, *59*, 23476−23479. (g) Zhu, D.; Qu, Z.-W.; Zhou, J.; Stephan, D. W. The Reactivity of Isomeric Nitrenium Lewis Acids with Phosphines, Carbenes, and Phosphide. *Chem. -Eur. J.* **2021**, *27*, 2861−2867. (h) Koronatov, A.; Mauda, A.; Tumansky, B.; Kaushansky, A.; Fridman, N.; Bravo-Zhivotovskii, D.; Gandelman, M. Multimodal Reactivity of N−H Bonds in Triazanes and Isolation of a Triazinyl Radical. *J. Am. Chem. Soc.* **2022**, *144*, 23642−23648.

(2) Mehta, M.; Goicoechea, J. M. Nitrenium Salts in Lewis Acid Catalysis. *Angew. Chem., Int. Ed.* **2020**, *59*, 2715−2719.

(3) (a) Ranolia, D.; Avigdori, I.; Singh, K.; Koronatov, A.; Fridman, N.; Gandelman, M. Triazolium Salts as Lewis Acid Catalysts. *Org. Lett.* **2022**, *24*, 3915−3919. (b) Singh, K.; Avigdori, I.; Kaushansky, A.; Fridman, N.; Toledano, D.; Gandelman, M. New Generation of Nitrenium Salts: Catalytic Hydrosilylation of Imines and a Mechanism of Action of Nitrogen Lewis Acids. *ACS Catal.* **2022**, *12*, 6831−6839.

(4) Danelzik, T.; Joseph, S.; Mück-Lichtenfeld, C.; Daniliuc, C. G.; García Mancheño, O. Benzotriazolium Salts: Emergent Readily Accessible Bench-Stable Lewis Acid Catalysts. *Org. Lett.* **2022**, *24*, 6105−6110.

(5) (a) Chen, K.-Q.; Zhang, B.-B.; Wang, Z.-X.; Chen, X.-Y. N-Heterocyclic Nitreniums Can Be Employed as Photoredox Catalysts for the Single-Electron Reduction of Aryl Halides. *Org. Lett.* **2022**, *24*, 4598−4602. (b) Bao, L.; Wang, Z.-X.; Chen, X.-Y. Photoinduced N-Heterocyclic Nitrenium-Catalyzed Single Electron Reduction of Acyl Fluorides for Phenanthridine Synthesis. *Org. Lett.* **2023**, *25*, 565−568. (c) Su, X.-D.; Yang, Z.-S.; Gong, W.; Wang, Z.-X.; Chen, X.-Y. Additive free, N-heterocyclic nitrenium catalyzed photoreduction of cycloketone oxime esters. *Org. Chem. Front.* **2023**, *10*, 1160−1165.

(6) (a) Liu, Q.; Zhang, B.-B.; Sheng, H.; Qiao, S.; Wang, Z.-X.; Chen, X. Visible-Light-Induced Photoreduction of Carborane Phosphonium Salts: Efficient Synthesis of Carborane-Oxindole-Pharmaceutical Hybrids. *Angew. Chem., Int. Ed.* **2023**, DOI: 10.1002/anie.202305088. (b) Ren, X.; Liu, Q.; Wang, Z.; Chen, X. Visible-light-induced direct hydrodifluoromethylation of alkenes with difluoromethyltriphenylphosphonium iodide salt. *Chin. Chem. Lett.* **2023**, *34*, 107473. (c) Liu, Q.; Lu, Y.; Sheng, H.; Zhang, C.-S.; Su, X.-D.; Wang, Z.-X.; Chen, X.-Y. Visible-Light-Induced Selective Photolysis of Phosphonium Iodide Salts for Monofluoromethylations. *Angew. Chem., Int. Ed.* **2021**, *60*, 25477−25484.

(7) (a) Scheiner, S. The Pnicogen Bond: Its Relation to Hydrogen, Halogen, and Other Noncovalent Bonds. *Acc. Chem. Res.* **2013**, *46*, 280−288. (b) Schmauck, J.; Breugst, M. The potential of pnicogen bonding for catalysis − a computational study. *Org. Biomol. Chem.* **2017**, *15*, 8037−8045. (c) Breugst, M.; Koenig, J. J. σ-Hole Interactions in Catalysis. *Eur. J. Org. Chem.* **2020**, *2020*, 5473−5487. (d) Mahmudov, K. T.; Gurbanov, A. V.; Aliyeva, V. A.; Resnati, G.; Pombeiro, A. J. Pnictogen bonding in coordination chemistry. *Coordin. Chem. Rev.* **2020**, *418*, 213381.

(8) (a) Yang, M.; Pati, N.; Bélanger-Chabot, G.; Hirai, M.; Gabbaï, F. P. Influence of the catalyst structure in the cycloaddition of isocyanates to oxiranes promoted by tetraarylstibonium cations. *Dalton Trans.* **2018**, *47*, 11843−11850. (b) Yang, M.; Tofan, D.; Chen, C.-H.; Jack, K. M.; Gabbaï, F. P. Digging the Sigma-Hole of Organoantimony Lewis Acids by Oxidation. *Angew. Chem., Int. Ed.* **2018**, *57*, 13868−13872. (c) Park, G.; Brock, D. J.; Pellois, J.-P.; Gabbaï, F. P. Heavy Pnictogenium Cations as Transmembrane Anion Transporters in Vesicles and Erythrocytes. *Chem.* **2019**, *5*, 2215−2227. (d) Yang, M.; Hirai, M.; Gabbaï, F. P. Phosphonium−stibonium and bis-stibonium cations as pnictogen-bonding catalysts for the transfer hydrogenation of quinolines. *Dalton Trans.* **2019**, *48*, 6685−6689. (e) Park, G.; Gabbaï, F. P. Redox-controlled chalcogen and pnictogen bonding: the case of a sulfonium/stibonium dication as a preanionophore for chloride anion transport. *Chem. Sci.* **2020**, *11*, 10107−10112. (f) Gonzalez, V. M.; Park, G.; Yang, M.; Gabbaï, F. P. Fluoride anion complexation and transport using a stibonium cation stabilized by an intramolecular P = O → Sb pnictogen bond. *Dalton Trans.* **2021**, *50*, 17897−17900.

(9) (a) Benz, S.; Poblador-Bahamonde, A. I.; Low-Ders, N.; Matile, S. Catalysis with Pnictogen, Chalcogen, and Halogen Bonds. *Angew. Chem., Int. Ed.* **2018**, *57*, 5408−5412. (b) Gini, A.; Paraja, M.; Galmés, B.; Besnard, C.; Poblador-Bahamonde, A. I.; Sakai, N.; Frontera, A.; Matile, S. Pnictogen-bonding catalysis: brevetoxin-type polyether cyclizations. *Chem. Sci.* **2020**, *11*, 7086−7091. (c) Paraja, M.; Gini, A.; Sakai, N.; Matile, S. Pnictogen-Bonding Catalysis: An Interactive Tool to Uncover Unorthodox Mechanisms in Polyether Cascade Cyclizations. *Chem. -Eur. J.* **2020**, *26*, 15471−15476. (d) Hao, X.; Li, T.-R.; Chen, H.; Gini, A.; Zhang, X.; Rosset, S.; Mazet, C.; Tiefenbacher, K.; Matile, S. Bioinspired Ether Cyclizations within a π-Basic Capsule Compared to Autocatalysis on π-Acidic Surfaces and Pnictogen-Bonding Catalysts. *Chem. -Eur. J.* **2021**, *27*, 12215−12223. (e) Humeniuk, H. V.; Gini, A.; Hao, X.; Coelho, F.; Sakai, N.; Matile, S. Pnictogen-Bonding Catalysis and Transport Combined: Polyether Transporters Made In Situ. *JACS Au* **2021**, *1*, 1588−1593.

(10) Zhang, J.; Wei, J.; Ding, W.-Y.; Li, S.; Xiang, S.-H.; Tan, B. Asymmetric Pnictogen-Bonding Catalysis: Transfer Hydrogenation by a Chiral Antimony(V) Cation/Anion Pair. *J. Am. Chem. Soc.* **2021**, *143*, 6382−6387.

(11) (a) Wang, H.; Wang, W.; Jin, W. J. σ-Hole Bond vs π-Hole Bond: A Comparison Based on Halogen Bond. *Chem. Rev.* **2016**, *116*, 5072−5104. (b) Toikka, Y. N.; Mikherdov, A. S.; Ivanov, D. M.; Mooibroek, T. J.; Bokach, N. A.; Kukushkin, V. Y. Cyanamides as π-Hole Donor Components of Structure-Directing (Cyanamide)···Arene Noncovalent Interactions. *Cryst. Growth Des.* **2020**, *20*, 4783−4793. (c) Ibrahim, M. A. A.; Rady, A. S. M.; Soliman, M. E. S.; Moustafa, M. F.; El-Mageed, H. R. A.; Moussa, N. A. M. π-hole interactions of group III−VI elements with π-systems and Lewis bases: a comparative study. *Struct. Chem.* **2022**, *33*, 9−21. (d) Calabrese, C.; Gou, Q.; Maris, A.; Caminati, W.; Melandri, S. Probing the Lone Pair···π-Hole Interaction in Perfluorinated Heteroaromatic Rings: The Rotational Spectrum of Pentafluoropyridine·Water. *J. Phys. Chem. Lett.* **2016**, *7*, 1513−1517. (e) Murray, J. S.; Lane, P.; Clark, T.; Riley, K. E.; Politzer, P. σ-Holes, π-holes and electrostatically-driven interactions. *J. Mol. Model.* **2012**, *18*, 541−548. (f) Bauzá, A.; Mooibroek, T. J.; Frontera, A. Directionality of π-holes in nitro compounds. *Chem. Commun.* **2015**, *51*, 1491−1493. (g) Báuza, A.; Frontera, A.; Mooibroek, T. J. π-Hole Interactions Involving Nitro Compounds: Directionality of Nitrate Esters. *Cryst. Growth Des.* **2016**, *16*, 5520−5524.

(12) (a) Müller, K.; Faeh, C.; Diederich, F. Fluorine in pharmaceuticals: looking beyond intuition. *Science* **2007**, *317*, 1881−1886. (b) Purser, S.; Moore, P. R.; Swallow, S.; Gouverneur, V. Fluorine in medicinal chemistry. *Chem. Soc. Rev.* **2008**, *37*, 320−330. (c) Zhou, Y.; Wang, J.; Gu, Z.; Wang, S.; Zhu, W.; Aceña, J. L.; Soloshonok, V. A.; Izawa, K.; Liu, H. Next Generation of Fluorine-Containing Pharmaceuticals, Compounds Currently in Phase II−III Clinical Trials of Major Pharmaceutical Companies: New Structural Trends and Therapeutic Areas. *Chem. Rev.* **2016**, *116*, 422−518.

(13) (a) Nagib, D. A.; MacMillan, D. W. C. Trifluoromethylation of arenes and heteroarenes by means of photoredox catalysis. *Nature* **2011**, *480*, 224−228. (b) Oh, S. H.; Malpani, Y. R.; Ha, N.; Jung, Y.-S.; Han, S. B. Vicinal difunctionalization of alkenes: chlorotrifluoromethylation with CF_3SO_2Cl by photoredox catalysis. *Org. Lett.* **2014**, *16*, 1310−1313. (c) Tang, X.-J.; Thomoson, C. S.; Dolbier, W. R. Photoredox-catalyzed tandem radical cyclization of N-arylacryla-

https://doi.org/10.1021/acs.orglett.3c02380
Org. Lett. 2023, 25, 6189−6194

mides: general methods to construct fluorinated 3,3-disubstituted 2-oxindoles using fluoroalkylsulfonyl chlorides. *Org. Lett.* **2014**, *16*, 4594−4597. (d) Tang, X.-J.; Dolbier, W. R. Efficient Cu-catalyzed Atom Transfer Radical Addition Reactions of Fluoroalkylsulfonyl Chlorides with Electron-deficient Alkenes Induced by Visible Light. *Angew. Chem., Int. Ed.* **2015**, *127*, 4320−4323.

(14) Zhou, F.; Liu, Y.-L.; Zhou, J. Catalytic Asymmetric Synthesis of Oxindoles Bearing a Tetrasubstituted Stereocenter at the C-3 Position. *Adv. Synth. Catal.* **2010**, *352*, 1381−1407.

(15) (a) Baya, M.; Joven-Sancho, D.; Alonso, P. J.; Orduna, J.; Menjon, B. M-C Bond Homolysis in Coinage-Metal $[M(CF_3)_4]^-$ Derivatives. *Angew. Chem., Int. Ed.* **2019**, *58*, 9954−9958. (b) Haire, L. D.; Krygsman, P. H.; Janzen, E. G.; Oehler, U. M. Correlation of radical structure with EPR spin adduct parameters: utility of the proton, carbon-13, and nitrogen-14 hyperfine splitting constants of aminoxyl adducts of PBN-nitronyl-13C for three-parameter scatter plots. *J. Org. Chem.* **1988**, *53*, 4535−4542.

(16) (a) Sun, X.; Wang, W.; Li, Y.; Ma, J.; Yu, S. Halogen-Bond-Promoted Double Radical Isocyanide Insertion under Visible-Light Irradiation: Synthesis of 2-Fluoroalkylated Quinoxalines. *Org. Lett.* **2016**, *18*, 4638−4641. (b) He, C.-L.; Wang, M.; Dong, B.-W.; Su, Y.-Q.; Duan, X.-H.; Liu, L. Lone pair-π interaction induced regioselective sulfonation of ethers under light irradiation. *Green Synth. Catal.* **2022**, DOI: 10.1016/j.gresc.2022.12.005. (c) Lu, J.; Khetrapal, N. S.; Johnson, J. A.; Zeng, X.; Zhang, J. "π-Hole-π" Interaction Promoted Photocatalytic Hydrodefluorination via Inner-Sphere Electron Transfer. *J. Am. Chem. Soc.* **2016**, *138*, 15805−15808.

Recommended by ACS

Photoinduced N-Heterocyclic Nitrenium-Catalyzed Single Electron Reduction of Acyl Fluorides for Phenanthridine Synthesis

Lei Bao, Xiang-Yu Chen, *et al.*

JANUARY 13, 2023
ORGANIC LETTERS

READ

Mechanism of Nitrogen-Carbon Bond Formation from Iron(IV) Disilylhydrazido Intermediates during N_2 Reduction

Samuel M. Bhutto, Patrick L. Holland, *et al.*

FEBRUARY 16, 2023
JOURNAL OF THE AMERICAN CHEMICAL SOCIETY

READ

Blue Light Irradiated Metal-, Oxidant-, and Base-Free Cross-Dehydrogenative Coupling of C(sp^2)–H and N–H Bonds: Amination of Naphthoquinones with Amines

Raushan Kumar Jha, Sangit Kumar, *et al.*

MAY 12, 2023
THE JOURNAL OF ORGANIC CHEMISTRY

READ

Study and Applications of Tetrasubstituted Hypervalent Selenium–Halogen Species in Catalytic Electrophilic Halogenations

Junjie Yang, Ying-Yeung Yeung, *et al.*

FEBRUARY 01, 2023
ACS CATALYSIS

READ

Get More Suggestions >

https://doi.org/10.1021/acs.orglett.3c02380
Org. Lett. 2023, 25, 6189−6194